INVESTIGATION OF HOLOGRAPHIC TESTING TECHNIQUES

Semiannual Report

1 June Through 27 November 1970

E. N. LEITH
C. M. VEST

February 1971

Willow Run Laboratories
INSTITUTE OF SCIENCE AND TECHNOLOGY

Prepared for the Advanced Research Projects Agency,
Department of Defense, Washington, D. C., ARPA
Order No. 1245, Program Code No. 8D10

Contract No. DAAG46-68-C-0017

NOTICES

Sponsorship. The work reported herein was conducted by the Willow Run Laboratories of the Institute of Science and Technology for the Advanced Research Projects Agency of the Department of Defense, ARPA Order No. 1245, Program Code No. 8D10, Contract No. DAAG46-69-C-0017. Contracts and grants to The University of Michigan for the support of sponsored research are administered through the Office of the Vice-President for Research.

Distribution. Initial distribution is indicated at the end of this document.

Final Disposition. After this document has served its purpose, it may be destroyed. Please do not return it to the Willow Run Laboratories.

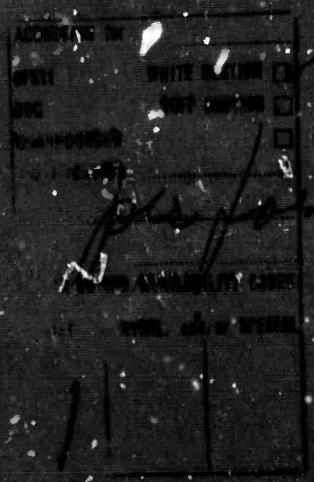

2420-21-P

INVESTIGATION OF HOLOGRAPHIC TESTING TECHNIQUES

Semiannual Report

1 June Through 27 November 1970

E. N. LEITH
C. M. VEST

February 1971

Radar and Optics Laboratory
Willow Run Laboratories
INSTITUTE OF SCIENCE AND TECHNOLOGY
THE UNIVERSITY OF MICHIGAN
Ann Arbor, Michigan

FOREWORD

This report was prepared by the Radar and Optics Laboratory of Willow Run Laboratories, a unit of The University of Michigan's Institute of Science and Technology, in conjunction with the Cooley Electronics Laboratory. The work was performed under ARPA-sponsored NDT Research Contract DAAG46-69-C-0017, which began 27 November 1968.

The report covers work performed between 1 June and 27 November 1970. The contract monitor is Mr. Robert C. Grubinskas, Nondestructive Testing Branch, Army Materials and Mechanics Research Center, Watertown, Massachusetts.

The Principal Investigators on this project are C. M. Vest and E. N. Leith. Sections 2 and 3 of this report were contributed by D. W. Sweeney and C. M. Vest. Section 4 was contributed by W. B. Ribbens, Section 5 by J. R. Varner, and Section 6 by D. C. Winter.

The work was submitted by the authors on 27 November 1970. The Willow Run Laboratories' report number is 2420-21-P.

This technical report has been reviewed and is approved.

ABSTRACT

This report discusses holographic schemes for the detection of flaws in honeycomb panels and also describes the development of a method of reducing the sensitivity of holographic interferometry of transparent objects. An interferometric scheme for determining the surface roughness of flat objects is presented, and a planned application of the technique to curved objects is discussed. Recent advances in multiple-frequency holographic contouring are described, and a comparison of holographic and shadow-moiré contouring schemes is presented. A computer simulation of acoustical holography and its use for reduction of aberration are also discussed.

CONTENTS

FIGURES

INVESTIGATION OF HOLOGRAPHIC TESTING TECHNIQUES
Semiannual Report
1 June Through 27 November 1970

1
INTRODUCTION

This is the fourth semiannual report on a continuing study of holographic testing techniques which began on 27 November 1968. This report presents technical accomplishments during the period from 1 June 1970 to 27 November 1970 and discusses preparatory work for the future investigation of holographic testing techniques.

In previous reports [1, 2, 3] we presented various applications of holographic interferometry to the nondestructive testing of materials. Here we discuss our search for an inspection technique which would locate disbonds in composite panels used as energy-absorbing cargo pallets. A variety of techniques for loading the specimen to induce interferometric fringe patterns which are indicative of bond flaws were tried. A satisfactory technique has not yet been developed. Plans for continuation of this effort are noted.

A preliminary investigation of a method to vary the sensitivity of interferograms of transparent objects was discussed in the last semiannual report [3]. This has been explored further and experimental results are presented here.

An optical technique for direct determination of rms surface roughness was shown to be feasible. The work reported here was based on the use of a Michelson interferometer and is applicable only to the study of flat surfaces. It is proposed to extend this technique to the inspection of surfaces of complex shape by using holographic interferometry.

Work on multiple-frequency holographic contouring is continuing. Investigations were conducted in order to learn why the high quality contour maps produced with the object physically close to the hologram [3] could not be reproduced when the object was imaged onto the hologram.

Computer simulation was used to learn what recording geometries minimize the aberrations in acoustic holography. The aberrations studied are inherent in acoustical holography because of the large difference in the wavelengths of radiation used during recording and reconstruction of the holograms. These aberrations are one of the major problems in development of ultrasonic holographic testing techniques.

BLANK PAGE

2
HOLOGRAPHIC TESTING OF AIRCRAFT LOADING PANELS

2.1. INTRODUCTION

In this section we present preliminary results of the holographic testing of a composite material. The material specimen is an aircraft loading panel which is used as an energy-absorbing cargo pallet. The core of this particular type of loading pad is heavy water-resistant paper; the skin is a thin aluminum sheet bonded to the paper core with an adhesive. The tests were carried out with the cooperation of Mr. Morris Budnick and Mr. Edward A. Nebesky, of the U. S. Army Natick Laboratories, who suggested the problem and made the panels available to us.

One of the most successful applications of nondestructive holographic testing has been debond detection in composite materials. Previous work on the inspection of aircraft trim tabs has been described in our earlier reports [2, 3]. In Ref. [3], the results of the holographic tests are compared with other nondestructive methods such as ultrasonic and radiographic techniques. The report concluded that the holographic technique of locating bond defects in an actual aircraft component appeared to be comparable with ultrasonic and radiographic techniques. Unfortunately, the success of holographic testing depends on whether the interior defects in a part can be made to perturb surface displacements locally. When the defects do perturb the surface displacements, the defects are revealed through anomalies in the resulting interferograms, which are qualitatively interpreted to determine defect size and location. Although the fringe anomalies may be quite visible, interpretation of defect size is an estimate based on the apparent extent of the fringe perturbations and the past experience of the operator. In practice, it seems reasonable to expect an error of less than 25% in estimated defect dimensions.

Since the results of this type of interferometric inspection are extremely dependent on the size, shape, and mechanical properties of the specimen, on the nature and size of the defect, and on the method of loading, it is difficult to make general statements regarding its applicability. Each specific application must be considered to determine if a viable test can be developed. For this reason, it is not unexpected that the aircraft trim tab experiments were successful while tests on other composite material [e.g., Ref. 3] produced only marginal results.

The intent of this investigation is to determine if a dependable and rapid holographic testing technique can be devised to locate bond defects in aircraft loading panels. The results obtained during this reporting period are compared with the tap technique used currently to test the panels. Plans for further tests are discussed.

2.2. EXPERIMENTAL PROCEDURE AND RESULTS

A typical experimental layout is shown in Fig. 1; this setup is a standard holographic system in which an object beam and reference beam simultaneously strike a photographic plate to produce the hologram. The system can be used for either real-time or double-exposure interferometry. In our experiments, the surface of the loading panel was painted white to produce a highly reflecting diffuse surface. Generally, the surface does not have to be painted. It was done in this case to decrease exposure times; exposure times of the painted surfaces were on the order of 30 sec for Kodak 649-F plates when a Spectra Physics 125 He-Ne laser was used as the light source to illuminate a circular test area of about 200 $in.^2$ on the specimen (8-in. diameter). Instead of painting the surface, faster photographic plates could be used (such as Agfa-Gevaert 10E75 which furnishes a 20-fold exposure reduction) or a stronger laser (such as a pulsed ruby laser or an argon gas laser). Once we have devised a viable testing method, we will investigate the applicability of the test to unpainted surfaces.

Figure 2 shows a typical loading panel. The test specimens have a surface area of roughly 2 ft^2; they are 2.1 in. thick, and the aluminum skin is 0.05 in. thick. The honeycomb-shaped cone is made of water-migration-resistant paper with a cell density of approximately 225 cells/ft^2.

Since specimens with standardized defects were not available when the tests began, it was necessary to introduce bond defects artificially. This was done by forcing a fine saw blade into the paper honeycomb as close to the aluminum skin as possible. The defect area is outlined with tape in Fig. 2. The broader section of the defect near the bottom of the panel is approximately 0.2 in. thick, while the upper portion of the defect is roughly 0.05 in. thick.

The back surface of the specimen was firmly attached to a heavy stand which allowed the front surface to deform freely under static or vibrational loading without the distorting effects of the loading fixture.

As mentioned above, the optimum loading technique used to distort the test specimen varies from application to application. In these experiments, thermal, static, and vibrational loads were tried. All three had some degree of success.

Marginal results were obtained by heating the back surface of the loading pad with an infrared lamp. The heat from the lamp was transmitted to the front surface skin of the panel and varied the temperature in the panel. Since surface strain in the skin is related to temperature variations in the structure, subsurface defects can be detected only if they sufficiently affect the thermal strain pattern on or near the surface Figure 3 shows a typical fringe pattern. The wider portion of the defect produced anomalies in the fringe pattern, but the more narrow portions of the defect did not. Apparently the thermal and mechanical properties

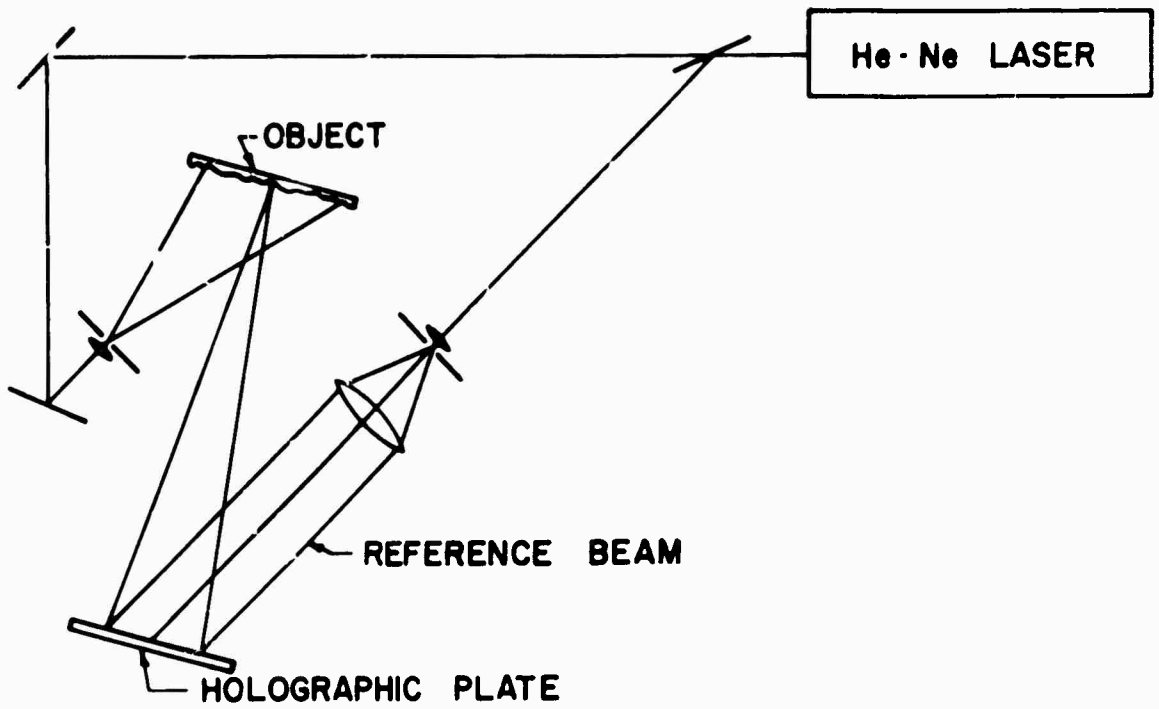

FIGURE 1. EXPERIMENTAL ARRANGEMENT FOR TESTING HONEYCOMB PANELS BY HOLOGRAPHIC INTERFEROMETRY

FIGURE 2. PHOTOGRAPH OF LOADING PANEL. The defective area is outlined.

FIGURE 3. FRINGE PATTERN PRODUCED BY HEATING THE PANEL FROM BEHIND

of this composite material are such that the thin voids in the adhesive or core material do not produce differential displacements of the aluminum skin.

Vibrating the front surface of the panel with a piezo-electric transducer produced the holograms shown in Figs. 4 and 5. When a hologram of a vibrating object is made (i.e., a time-average hologram), the hologram produces an image of the original vibrating object with a set of fringes superimposed on the image. The fringe pattern reveals the shape and amplitude of the vibrational pattern. For the simple case of vibration normal to the direction of observation, the intensity of any given point within the fringe pattern is proportional to the zero-order Bessel function; that is

$$I \sim \left| J_0\left(\frac{4\pi}{\lambda} d\right)\right|^2$$

where d is the total amplitude of vibration, and λ is the wavelength of the laser light.

In these tests the front surface of the transducer was held against the panel with a heavy steel bar suspended in front of the panel; the front surface of the transducer which was pressed against the panel was 0.5 in. in diameter. The transducer was excited with a single-frequency oscillator at 600 cycles/sec. Other frequencies were tried but this frequency seemed to produce a resonant mode in the panel.

Again, the objective was to locate anomalies in the time-average fringes caused by perturbations of the vibrational mode of the panel due to the defects. Figure 4 shows a time-average hologram of the panel when the transducer is placed directly over the defect. The fringe pattern reveals a region of locally high vibrational amplitude due to the defect. Figure 5 shows another time-average hologram made with the transducer 4 in. to the left of the defect. This hologram shows no region of local vibration.

The results of the vibrational technique seem to be reliable; they give a clear indication of the presence of a defect. However, the technique has two disadvantages. First, the total defect area is not shown. Figure 4 indicates a defect, but there is no indication of its size or shape. It would, of course, be desirable to determine the full extent of the debonds. Second, defect location for a large panel would require a point-by-point scan. One of the primary advantages of holographic testing is the ability to test large surface areas at one time. It appears that although vibrational techniques may eventually be successful, some modifications must be made to give a single map of the location and size of defect areas for large surface areas.

Figures 6 and 7 are reconstructions of multiple-exposure holograms produced by static loading. In these experiments a hemispherical probe was pressed against the front surface of the panel. A micrometer measured the displacements of the probe. The photographic plate was exposed three times instead of the usual two. It was first exposed with the probe pressing

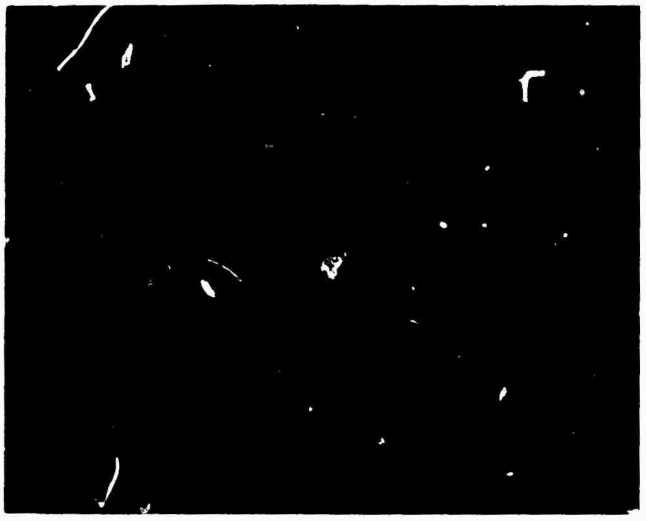

FIGURE 4. FRINGE PATTERN PRODUCED BY VIBRATING THE PANEL SURFACE WITH THE TRANSDUCER OVER THE DEFECT

FIGURE 5. FRINGE PATTERN PRODUCED BY VIBRATING THE PANEL SURFACE WITH THE TRANSDUCER TO THE LEFT OF THE DEFECT

FIGURE 6. MULTIPLE-EXPOSURE FRINGE PATTERN PRODUCED BY STATIC LOADING APPLIED TO THE LEFT OF THE DEFECT

FIGURE 7. MULTIPLE-EXPOSURE FRINGE PATTERN PRODUCED BY STATIC LOADING APPLIED OVER THE DEFECT

lightly against the front surface of the panel. With the probe 0.001 in. further into the panel surface, a second exposure was made. The probe was moved 0.001 in. more into the panel surface, and the plate was exposed a third time. This technique was first proposed by Burch and his colleagues [4]. The exposure time was increased 10% for each successive exposure, as suggested by Biedermann [5], to produce equally intense reconstructed images. Basically, each exposure pair produces a separate interferogram; the first and second, the second and third, and the first and third exposure pairs each produce a separate fringe pattern.

The three superimposed fringe patterns combine to form a moiré fringe pattern. If the displacements between exposures are all equal, all the fringe patterns have harmonically related fringe frequencies. The moiré fringe pattern produced by the interferometric fringes is the same as that produced by a double-exposure hologram made from only the first two exposures except that low-amplitude high-frequency fringes fall between the broader fringes. If the displacements between exposures are not equal, the resulting interferometric fringes do not beat together to form moiré fringes with high visibility as they did in the first case. The fringes tend to wash out and form patterns with varying visibility. This technique can be used to detect an object's nonlinear response to a deforming load by merely observing the visibility of the resulting fringes.

We used the above technique for our tests to determine if it would facilitate identification and to demonstrate an extension of double-exposure holography. This technique does not change the basic configuration of the fringe pattern, however, and in that sense the same results could be obtained using double-exposure holography.

Figure 6 shows a reconstruction of a multiple-exposure hologram; the probe is about 1 in. to the left of the defect. The moiré fringe pattern is clear and has high visibility. There is a slight change in the slopes of the fringes over the defect. The difference is so slight, however, that flaws probably cannot be detected reliably. Figure 7 shows a reconstruction when the probe is directly over the defect. The circular fringes around the probe indicate a subsurface defect. Over the remainder of the panel, the fringes are not nearly as clear as the fringes in Fig. 6, which indicates an unequal movement of this portion of the panel between the three exposures. Although Fig. 6 shows some indication of a defect not directly under the probe, it appears that a point-by-point scan is again required.

2.3. CONCLUSIONS AND PLANS FOR FURTHER INVESTIGATIONS

Of the three loading methods used, only vibrational and static loading appear to offer a chance of success. Both techniques presently require a point-by-point scan of the surface. The technique currently used to test the panels for debonds involves tapping the surface of the panel and detecting the audio response. This is a point-by-point technique also. Since the

audio response of the defect we introduced was clearly different from the response of other portions of the panel when tapped with a metal rod, it appears that the particular holographic techniques discussed here offer no clear advantages over the tap test methods. In order for the holographic techniques to be preferred, they will have to produce maps of a large surface area showing the size and location of all defects.

All of the tests do indicate, however, that the debonds produce a soft spot in the surface that deforms locally when it is compressed. To take advantage of this effect, a uniform fluid pressure or vacuum could be applied to the front panel surface and the entire surface then observed through a viewing window. This procedure will be attempted and results reported in the next report.

The U. S. Army Natick Laboratories have arranged for the U. S. Bureau of Standards to prepare panels identical to those being studied but with disbonds of various sizes introduced during manufacture. The bonding material, which was not removed in previous tests, is quite rigid in comparison with the paper core. The nature of the disbond may, therefore, greatly affect the results of holographic testing. These new specimens will allow us to assess holographic testing techniques for these panels more realistically.

3
INTERFEROMETRY OF THREE-DIMENSIONAL TRANSPARENT OBJECTS

3.1. INTRODUCTION

In our last semiannual report [3], we discussed two studies undertaken to expand the uses of holographic interferometry in the inspection of transparent objects. The first study concerned the use of multidirectional object illumination derived from a phase grating. This type of illumination enables us to produce holographic interferograms which could be viewed from several directions, but which were essentially free of the laser speckle problem associated with the more conventional diffuse object illumination. The second study dealt with a possible technique for reducing the sensitivity of holographic interferometry. This was accomplished by using a hologram formed by the interference of two light waves which pass through the object under study. Here we report on the further development and investigation of this technique.

3.2. DESENSITIZED INTERFEROMETRY

This section discusses an extension of holographic interferometry in which both waves used to record the hologram pass through the transparent object being studied. This technique has features which are unique and cannot be duplicated by classical interferometry. An interferometer of variable sensitivity is used which has a strong bias toward the detection of changes of phase in one direction.

Figure 8 depicts the optical arrangement for recording the hologram. Two coherent plane waves traverse a transparent object at slightly different angles. The resulting intensity pattern is recorded on film to form a hologram. No additional reference wave is used during this exposure. We will show below that if this hologram is reconstructed by one of the plane waves, the fringe pattern obtained by interfering this reconstructed wave with the other plane wave is indicative of the difference in optical path of the two waves which traversed the object. This technique is suggested by the method of holographic imaging through aberrating media developed by Goodman and his colleagues [6, 7]. They demonstrated that by placing a coherent point source very close to an object and recording a hologram, aberrations caused by refracting media between the object and the hologram plane are minimized since both the object and reference waves are aberrated in approximately the same manner. We have applied this concept to interferometry.

Let the two waves striking the hologram in Fig. 8 be denoted by

$$u_1 = a_1 \exp i[\alpha_1 x + \phi_1(x, y)] \tag{1a}$$

and

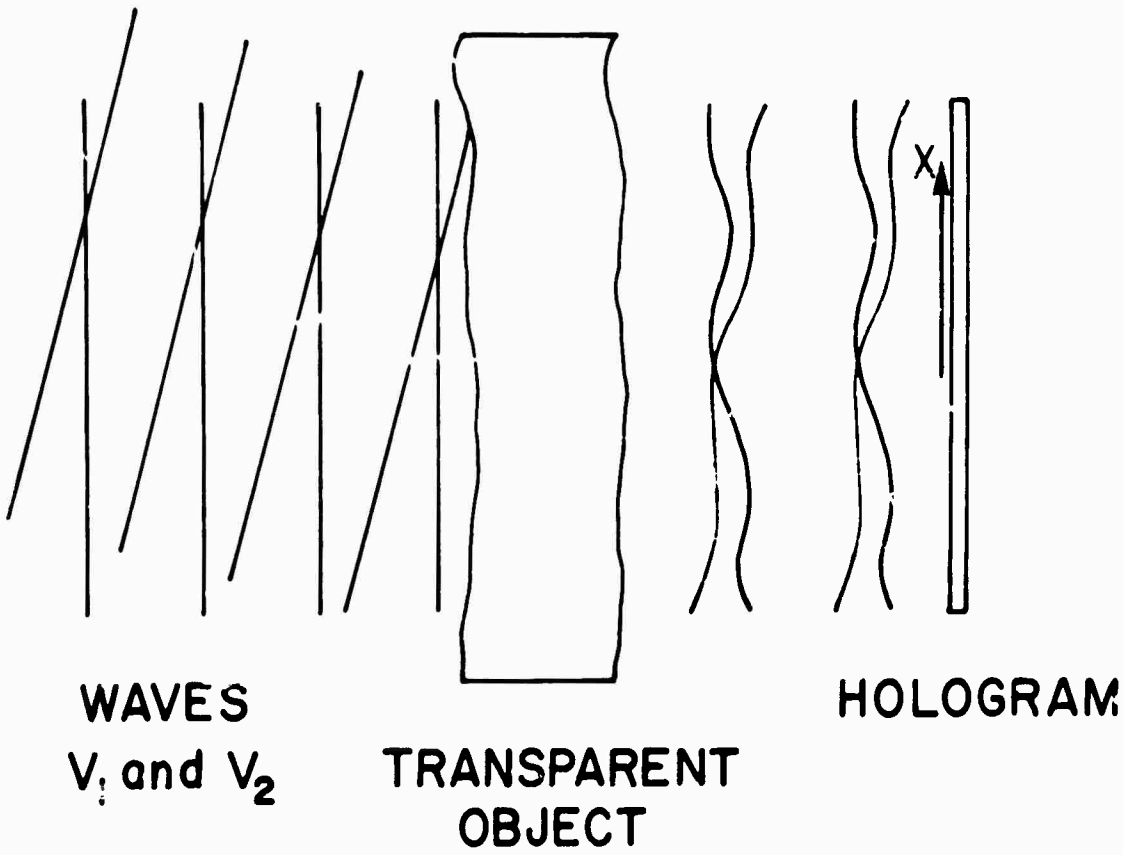

FIGURE 8. OPTICAL ARRANGEMENT FOR RECCRDING THE HOLOGRAM

$$u_2 = a_2 \exp i[\alpha_2 x + \phi_2(x, y)] \tag{1b}$$

where α_1 and α_2 are proportional to the angles of propagation of the waves, and $\phi_1(x, y)$ and $\phi_2(x, y)$ describe the phase variations introduced by the transparent object. As usual, the temporal variation has been suppressed. Let us further assume that $a_1 = a_2 = a$, which is uniform across the hologram plane. Under these assumptions, an ideal, linearly recorded hologram would have an amplitude transmittance of the form

$$t(x, y) = t_b + \beta\left(u_1 u_2^* + u_2 u_1^*\right) \tag{2}$$

If we reconstruct this hologram by illuminating it with a plane wave, $u_{1p} = a \exp i(\alpha_1 x)$, the reconstructed virtual wavefront would be

$$u_{2v} = \gamma a^3 \exp i(\alpha_2 x + \phi_2 - \phi_1) \tag{3}$$

If this reconstructed wavefront interferes with a plane wave $u_{2p} = \gamma a \exp i(\alpha_2 x)$, the resulting intensity is

$$I = K + 2\beta\gamma a^4 \cos(\phi_2 - \phi_1) \tag{4}$$

where K is a constant and γ is an attenuation factor. This interference pattern is only indicative of $\delta\phi = \phi_2(x, y) - \phi_1(x, y)$, which is the difference in phase variations introduced into the plane waves traversing the object in different angular directions.

The most obvious feature of this interferometer is that its sensitivity can be low; it can produce very low frequency fringes in comparison with those produced for the same object by, say, a Mach-Zehnder interferometer. It may, therefore, be applied to the study of quite coarse phase objects. The interferometer is also more sensitive to phase variations in the x-direction than in the y-direction. If one considers two rays traversing the object and converging to the point on the film at which they interfere to form the hologram, it is obvious that this interferometer is most sensitive to gradients of refractive index in planes far from the hologram where the rays are considerably separated from each other. The interferometer is least sensitive very close to the hologram where the rays nearly coincide. The region of low sensitivity could be shifted along the z-axis by placing an imaging lens between the object and the hologram. This feature may be useful for studying the structure of three-dimensional phase objects. For this application, the two-hologram technique suggested by Bryngdahl and Lohmann [8] together with Goodman's holographic imaging scheme could be used to advantage.

We have conducted experiments which demonstrate several of the predicted features of this technique. Two coherent plane waves were generated with an optical setup similar to a Michelson interferometer. All holograms were recorded on Kodak 649-F spectroscopic

plates with 6328-Å light. Figure 9 shows three interferograms of the same transparent object (a sheet of plexiglass, 0.635 cm thick). Figure 9a was produced by the method described above. The angle between the beams was 1^{o}, and the object was located about 3.2 cm in front of the hologram. The fringe pattern in Fig. 9b was produced by placing the object in a Mach-Zehnder interferometer also with 6328-Å light. Note that the fringes in Fig. 9a are indeed coarse and tend to emphasize lateral variation of phase (i.e., are indicative of the gradient of phase in the lateral direction) compared with those in Fig. 9b. The fringes in Fig. 9c were produced as in 9a, except the object was rotated 90^{o} in the x, y plane.

The ability to vary the sensitivity of this interferometer is further illustrated by Fig. 10. The interferogram shown in Fig. 10a was produced in the same manner as that in Fig. 9a, except the angle between the beams was 3^{o} rather than 1^{o}; hence, the fringes in Fig. 10a are more numerous than those in Fig. 9a. Figures 10b and 9c may be compared in an analogous manner.

For simplicity and ease of adjustment during the experiments reported here, a double-exposure technique was used. During the first exposure, both waves passed through the object and exposed the film. The object was then removed and the film was exposed to the two plane waves. The second recording simply provided a hologram of the wave u_{2p} which is required to form the final interference pattern. Readout then consisted of illuminating the developed hologram with the other plane wave, u_{1p}, Fourier transforming the output of the hologram with a spherical lens, and filtering out the unwanted spectral components. It should be noted that the angle between the waves which form the hologram is sufficiently small that both the real and virtual holographic images appear upon reconstruction [9]. It is easily shown that the same interference pattern is obtained using the virtual image. This has been verified experimentally.

The basic properties of the interferometer were clearly illustrated by using a thin (9^{o} wedge) prism as an object. Figure 11a is an interferogram produced using the method under consideration. One wave was parallel to the front face of the prism and the other was tilted at an angle of 1^{o}. The prism, with its wedge in the x, y plane, was located 5 cm in front of the hologram. The resulting fringe frequency is about 4 lines/cm. The fringes shown in Fig. 11b were produced using the same setup, but there was a 5^{o} angle between the beams. The resulting fringe frequency is 22 lines/cm. The absolute fringe frequency due to refraction by the prism was measured by placing the prism in a portion of a collimated beam. The interference between the refracted and unrefracted portions of the beam was recorded on film. The resulting fringe frequency was found with a scanning microdensitometer to be 135 lines/mm. When the prism was turned 90^{o} so that the wedge lay in the y, z plane, no fringes were produced, since no x gradient of phase was introduced. It is interesting to note that the fringes produced

(a) Desensitized Interferogram. Beam angle = 1°.

(b) Bright-Field Mach-Zehnder Interferogram.

(c) Desensitized Interferogram. Object rotated 90° during recording.

FIGURE 9. THREE INTERFEROGRAMS OF THE SAME PORTION OF A TRANSPARENT OBJECT

(a) Desensitized Interferogram. Beam angle = 3^{o}.

(b) Desensitized Interferogram. Object rotated 90^{o} during recording.

FIGURE 10. TWO INTERFEROGRAMS OF THE SAME PORTION OF THE TRANSPARENT OBJECT IN FIG. 9

(a) Beam Angle = 1^{o}

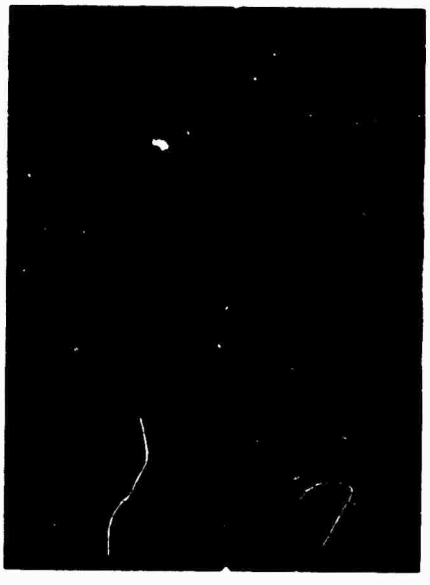

(b) Beam Angle = 5^{o}

FIGURE 11. TWO INTERFEROGRAMS OF A 9^{o} WEDGE PRISM

by this interferometer are indicative of deviations from the thin prism approximation. In this approximation, the linear phase shift introduced by the prism is independent of the angle of incidence. If this were indeed the case, no fringes would be produced by this interferometer.

In conclusion, we suggest that the concept of perturbing both the object and reference waves may lead to interesting new methods and applications of holographic interferometry. We have illustrated this in terms of a particular interferometer. For thin phase objects, the output of this interferometer is nearly analogous to that of a shearing interferometer. For phase objects of greater thickness, the results could be duplicated only by physically rotating the object between exposures in ordinary two-exposure holographic interferometry. This would be impossible if the refractive index distribution under study varies with time.

4
OPTICAL MEASUREMENT OF SURFACE ROUGHNESS

4.1. INTRODUCTION

The purpose of this facet of the investigation is to establish the feasibility of measuring surface roughness by means of optical interferometry. We examined the interference pattern formed by the superposition of light beams reflected from a test surface to be measured and a reference surface which is assumed to be perfectly smooth.

It has long been understood that the interference fringe contrast ratio is influenced by the mutual coherence of the two interfering beams. In this study the influence of the roughness of the test surface on the mutual coherence of the interfering beams is investigated theoretically and experimentally. A definite relationship has been established between the fringe contrast ratio and the rms surface roughness.

In the initial phases of this study a Michelson interferometer configuration has provided the interference pattern. However, in the next quarterly research period, holographic interferometry will be applied to this problem. The Michelson interferometer is strictly limited to the study of surfaces which are flat to within a few optical wavelengths. However, holographic interferometry is applicable to a variety of object shapes and should provide a more versatile tool for roughness measurement. In this section the theory of this surface roughness measurement scheme is explained in terms of the Michelson configuration, and experimental results are presented.

4.2. THEORY OF THE TECHNIQUE

The conceptual basis of the present method is illustrated by Fig. 12, which is a schematic drawing of the instrumentation used. The instrument is essentially an interferometer, one of whose faces is the surface under study (this is assumed to be nearly flat). The light from the laser is split into two components which are reflected from a reference surface and the test surface (i.e., u_r and u_s, respectively) and recombined. An interference pattern is formed by the recombination of these two light components; the fringe contrast ratio is determined by the mutual coherence of the two wavefronts. Assuming that the laser output is perfectly monochromatic, then the mutual coherence of the two wavefronts is determined by the roughness of the test surface and the reference mirror. Although the reference mirror can be considered perfectly flat and smooth, the test surface produces a reflected wave which is randomly phased. Thus, both the mutual coherence between the wavefronts reflected from the test and reference surfaces and the fringe contrast ratio are reduced by the roughness of the test surface.

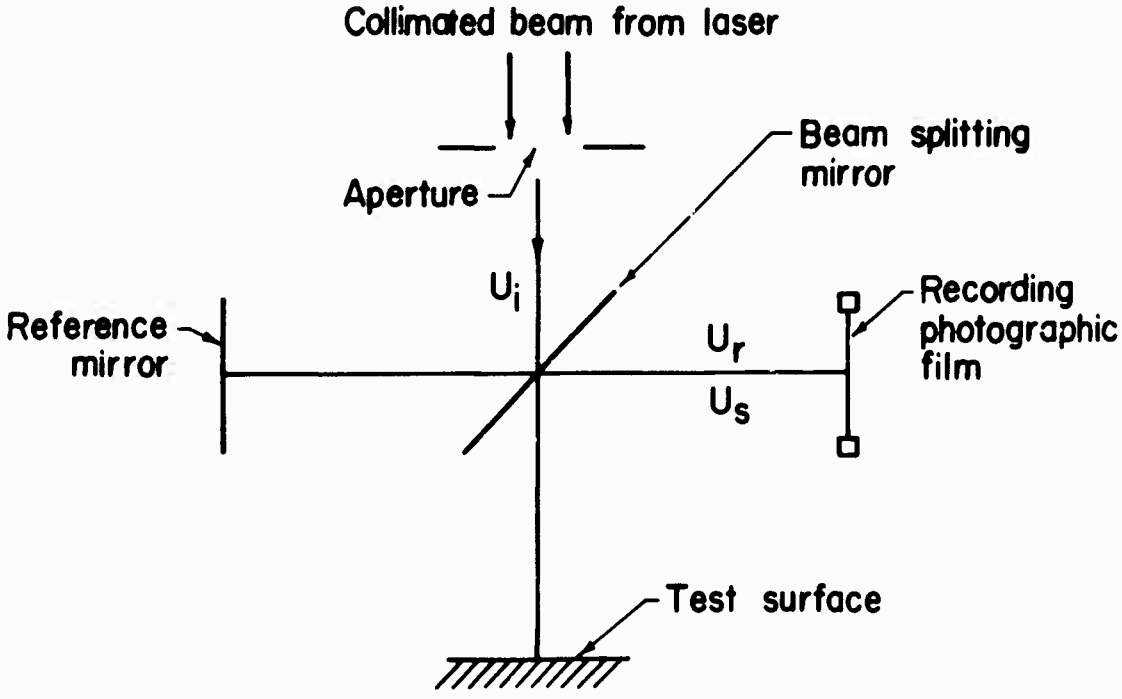

FIGURE 12. DIAGRAM OF INSTRUMENTATION USED IN ROUGHNESS MEASUREMENT

Below we will develop the correlation between surface roughness and fringe contrast ratio which allows us to use a measurement of fringe contrast to measure surface roughness. For this purpose it is appropriate to compute the interference pattern obtained in the configuration of Fig. 12 and to study the relationship of surface roughness to this pattern. The interference pattern is determined by the superposition of the light amplitude components u_r and u_s. It is shown in Ref. [10] that these light components are related to the incident light amplitude u_i, which includes the pupil function, by the expression

$$u_{r,s} = \frac{\exp i\phi_{r,s}}{4\lambda R_{r,s}} \int_{-\infty}^{\infty}\int [\rho_{r,s} u_i(x_1 y_1)] \times \exp j\left[kz(x_1 y_1) + \frac{2\pi}{\lambda R_{r,s}}(x_0 x_1 + y_0 y_1)\right] dx_1 dy_1 \qquad (5)$$

where x_1 and y_1 are the coordinates in the plane of these surfaces, and z is the coordinate representing the instant height of the surface relative to the mean surface (i.e., z = 0). The phase of the two light components $\phi_{r,s}$ is determined by the distances $R_{r,s}$ from the mean surfaces to the photographic plate and the light wavelength λ. The variables x_0 and y_0 are the coordinates in the plane of the photographic plate, and $\rho_{r,s}$ are the complex reflectivity of the reference and test surfaces, respectively.

In writing Eq. (5) for these light components, the following significant assumptions are made:

(1) The angle between the normal to the test surface and the incident light propagation vector is approximately zero.

(2) The total phase from each point on the test surface to each point on the observation plane is represented in the Fraunhofer approximation.

(3) Shadowing of parts of the surface can be neglected. These assumptions tend to be valid for relatively smooth surfaces and are usually not valid for surfaces where roughness exceeds optical wavelength.

A number of observations can be made which simplify the above expressions for u_r and u_s. The reference surface is assumed to be smooth, which means that $z(x_1 y_1) \equiv 0$ on the reference surface. In addition, the interferometer is constructed so that $R_r \cong R_s = R_0$, thereby greatly simplifying the expressions for the light components. Because the film recording process is nonlinear, it is the fringe intensity pattern I which is recorded on the film:

$$I = \left| K \iint_{\text{aperture}} dx_1 dy_1 \, F(x_1 y_1)\left[\rho e^{i\phi} + \exp ikz(x_1 y_1)\right] \right|^2 \qquad (6)$$

where

$$\phi = \phi_r - \phi_s$$

and

$$F = u_i \exp i\frac{2\pi}{\lambda R_0}(x_0x_1 + y_0y_1)$$

and ρ is the ratio of reflectivities of the reference and test surfaces. It has been assumed that the light components, after being separated at the beam splitter, encounter identical apertures at both surfaces.

The relationship between Eq. (6) and the surface roughness is found using standard procedures for computing expected values. First we make the following observations:

$$\frac{I}{|K|^2} = \left|\iint_{\text{aperture}} dx_1\,dy_1\,F(\rho e^{i\phi} + e^{iks})\right|^2$$

$$= \iint_{\text{aperture}} dx_1\,dy_1 \iint_{\text{aperture}} dx_1'\,dy_1'\,FF'[(\rho\cos\phi + \cos kz)(\rho\cos\phi + \cos kz')$$

$$+ (\rho\cos\phi + \sin kz)(\rho\sin\phi + \sin kz')] \qquad (7)$$

where

$$z' = z(x_1'y_1')$$

and

$$F' = F(x_1'x_1')^*$$

and where the integrals are taken over the aperture. Using this notation, Eq. (7) can be written in the following form

$$\frac{I}{|K|^2} = \iint_{\text{aperture}} dx_1\,dy_1 \iint_{\text{aperture}} dx_1'\,dy_1'\,FF'$$

$$\{\rho^2 + \rho[\cos\phi\,(\cos kz' + \cos kz) + \sin\phi\,(\sin kz + \sin kz')] + \cos k(z - z')\} \qquad (8)$$

The important quantity statistically is the average value of the intensity I. The average is considered to be taken over an ensemble of statistically identical reflectors (or equivalently over several portions of the surface under study). It is assumed that the ensemble average is the same as the space average

$$E\left(\frac{I}{|K|^2}\right) = E\iint f(x, y, z)\,dx\,dy = \iint Ef(x, y, z)\,dx\,dy$$

The expected value of this ratio can be computed if the following assumptions are made: (1) the statistics of z are known (zero mean); and (2) the ensemble average equals the space average.

Making these assumptions and assuming Gaussian statistics leads to the following expression for the expected value of $I/|K|^2$ [see Ref. 11]:

$$E\left(\frac{I}{|K|^2}\right) = \iint dx_1\,dy_1 \iint dx_1'\,dy_1'\,FF'(\rho^2 + 2\rho\cos\phi \exp\left(\frac{-k^2\sigma^2}{2}\right)$$

$$+ \exp -k^2\sigma^2\{1 - R[(x_1 - x_1'), (y_1 - y_1')]\} \qquad (9)$$

where R is the autocorrelation function for z. In Eq. (9) σ is the standard deviation of z, which is the rms surface roughness to be measured. This expression can be evaluated approximately by neglecting the contribution R to the value of the integral. It should be noted that $0 \leq R \leq 1$ and that R differs from zero for only a short range of $x_1 - x_1'$, $y_1 - y_1'$. Thus, the error in neglecting this term is made arbitrarily small by making the aperture arbitrarily large. The approximate value for $E\left(\frac{I}{|K|^2}\right)$ is given by

$$E\left(\frac{I}{|K|^2}\right) = \left(\rho^2 + 2\rho\cos\phi \exp -\frac{k^2\sigma^2}{2} + \exp -k^2\sigma^2\right)\left(\iint_{\text{aperture}} dx_1\,dy_1 F\right)^2 \qquad (10)$$

The characteristics of the fringe pattern can be understood by interpreting Eq. (10). The integral in the second factor is proportional to the light intensity distribution in the observation plane when the test surface is removed. The value of the first factor depends upon interferometer alignment. If the interferometer is perfectly aligned (i.e., if test and reference surfaces are exactly flat and perpendicular), a uniform light pattern results. The intensity of this light pattern will increase and decrease as the position of the reference mirror is changed in the z direction. A maximum light intensity is obtained for $\phi = (2N + 1)\pi$, where N is any integer.

On the other hand, if the interferometer is misaligned slightly, a coarse fringe pattern is obtained. In this case ϕ is a function of the coordinates x_0, y_0. The maximum intensity occurs whenever $\phi = 2N\pi$, and the minimum intensity occurs wherever $\phi = (2N + 1)\pi$. The fringe contrast ratio R is the ratio of the maximum light intensity to the minimum intensity as expressed by the relation:

$$R = \frac{E\left(\frac{I}{|K|^2}\right)_{max}}{E\left(\frac{I}{|K|^2}\right)_{min}} = \frac{E(\phi)_{\phi = 0}}{E(\phi)_{\phi = \pi}} \tag{11}$$

$$R = \frac{\rho^2 + 2\rho \exp\left(-\frac{k^2\sigma^2}{2}\right) + \exp\left(-k^2\sigma^2\right)}{\rho^2 - 2\rho \exp\left(-\frac{k^2\sigma^2}{2}\right) + \exp\left(-k^2\sigma^2\right)} = \frac{\rho + \exp\left(-\frac{k^2\sigma^2}{2}\right)^2}{\rho - \exp\left(-\frac{k^2\sigma^2}{2}\right)}$$

Solving Eq. (11) for the rms surface roughness σ yields

$$k\sigma = \frac{2\pi\sigma}{\lambda} = \frac{1}{2} \log_e \left[\frac{(R+1)^{1/2}}{\rho(R-1)^{1/2}}\right] \tag{12}$$

Using this relationship, the rms surface roughness σ can be found by measuring the fringe contrast ratio R.

4.3. EXPERIMENTAL RESULTS

Experimental support of this theory has been obtained in several cases using this method and comparing the results with surface roughness measured using a stylus instrument. A photographic plate is exposed to this interference pattern to obtain a record of the intensity distribution. In the experimental work the film density was measured using a microdensitometer and was converted to light intensity from which the fringe contrast ratio was obtained.

Figure 13 contains a pair of photographs taken from two different surfaces which illustrate typical fringe patterns. Figure 13a is taken from a surface with a 0.5-μin rms roughness, and Fig. 13b is taken from a surface with a 5-μin. rms roughness.

As an example of the accuracy of this method, we measured the roughness of a steel test surface which had been lapped to a roughness of 3 μin. (0.075 μm, as measured on a stylus instrument). Converting the measured fringe contrast ratio to surface roughness yields σ = 3.2 μin. (0.082 μm).

A number of surfaces with different surface roughnesses have been measured using this interferometric technique. The specimens for all experiments were 2-in. steel disks. The surface area illuminated on each sample was approximately 1 cm in diameter. The surface roughness values measured this way have been compared with those obtained with a stylus instrument. For the purpose of comparing these two measurements, the following relative error is defined:

(a) rms Roughness = 0.5 μin.

(b) rms Roughness = 5 μin.

FIGURE 13. REPRESENTATIVE EXAMPLES OF INTERFERENCE FRINGE PATTERNS FOR VARIOUS SURFACES

$$\zeta = \frac{|r_l - r_s|}{r_s}$$

where r_l = rms roughness determined by the interferometric method, and r_s = rms roughness determined by stylus instrument.

The Table is a comparison of rms surface roughness measured by the stylus and by the interferometric method. The fractional error is presented as a numerical comparison. However, the significance of the comparison between these two measured values is strongly influenced by the characteristics of the stylus instrument. The variation in successive measurements made on the same surface with the stylus instrument is of the same order as this fractional error. Moreover, the calibration accuracy of any stylus instrument is subject to considerable doubt. Thus, a large fractional error does not necessarily indicate a large error in the interferometric surface roughness measurement.

The relative error increases for surfaces with an rms roughness greater than about 5 μin. (0.127 μm). The stylus instrument is believed to be increasingly accurate in this region of roughness beyond 5-μin. rms. It is reasonable to conclude, therefore, that the interferometric roughness measurement is not valid beyond 5 μin. for this optical wavelength $\left(\text{i.e., } \frac{\sigma}{\lambda} \sim \frac{1}{5}\right)$. It is reasonable to conclude, moreover, that this upper limit to surface roughness will increase in proportion to the optical wavelength. Thus, the range of surface roughness which can be accurately determined using this interferometric method is nominally 10 Å $\leq r \leq \frac{\lambda}{5}$ for an optical wavelength λ.

4.4. PLANS FOR EXTENSION TO HOLOGRAPHIC INTERFEROMETRY

Although the principle of interferometric surface roughness measurement has been developed only for a Michelson interferometer, the mathematical relationship between surface roughness and fringe contrast ratio is similar for all interferometry. During the next research period, the application of holographic interferometry to surface roughness measurement will be investigated both experimentally and theoretically. The configuration for this study is shown in Fig. 14.

A hologram of a reference surface (i.e., assumed to be perfectly smooth) is made with the reference surface occupying the position of the test surface as shown in Fig. 14. Then the reference surface will be replaced by a test surface (both surfaces are approximately flat). Every effort will be made to maintain registration between the hologram and the location of the reference/test surface. The contrast ratio of the interference fringes in the observation plane will be studied theoretically and experimentally.

TABLE. COMPARISON OF STYLUS AND INTERFEROMETRIC SURFACE ROUGHNESS MEASUREMENTS

rms Roughness (Stylus) (μin.)	rms Roughness (Interferometric) (μin.)	ζ
1.0	0.95	0.05
3.1	3.2	0.3
5.0	4.5	0.1
8.2	6.9	0.16
10.0	7.8	0.22
16.0	10.4	0.24

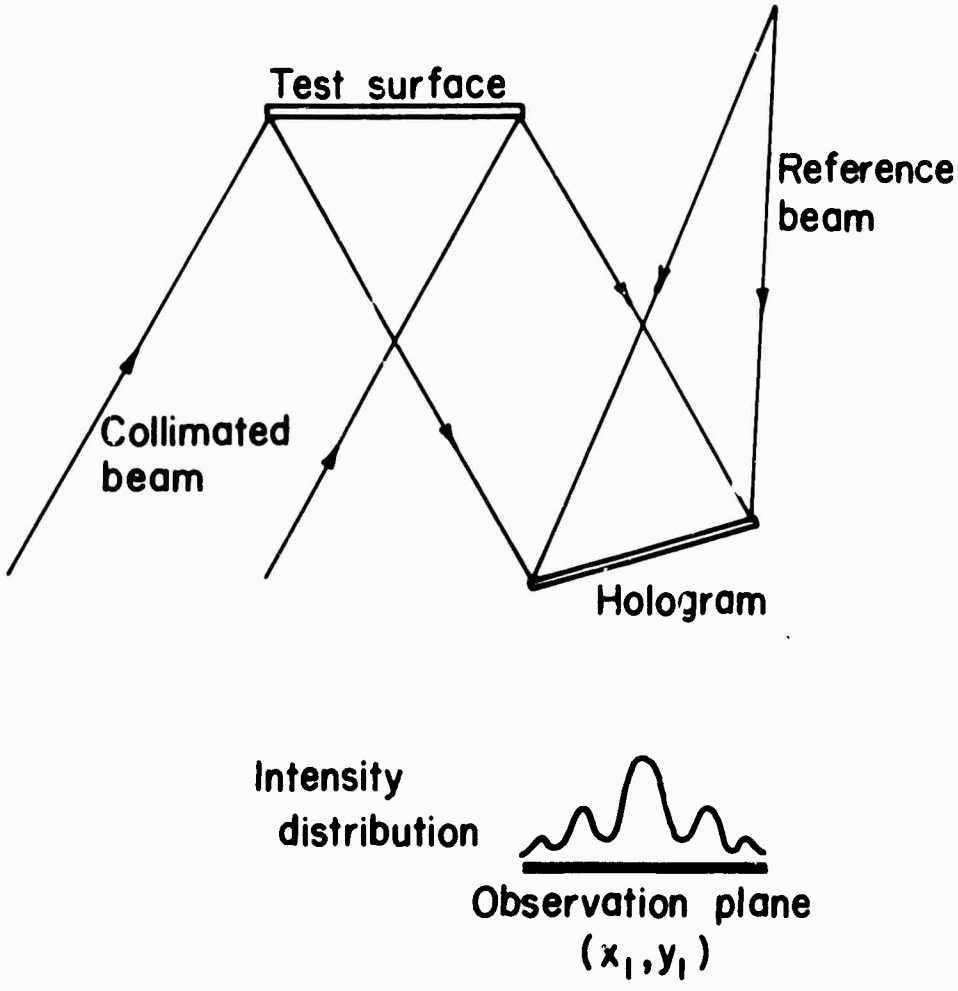

FIGURE 14. HOLOGRAPHIC INTERFEROMETRY CONFIGURATION FOR SURFACE ROUGHNESS MEASUREMENT

Although it is expected that holographic interferometry will be applicable to the study of surface roughness for objects of complex shape, the initial experiments will be performed on flat surfaces. These surfaces are the same ones studied in the Michelson configuration and will provide a comparison between theory and experiment for known surfaces.

5
HOLOGRAPHIC CONTOURING

5.1. INTRODUCTION

Previous reports [2, 3] have contained descriptions of two multiple-frequency contouring techniques based on near-image-plane holography. These are:

(1) Holographic contouring with auxiliary imaging systems [Ref. 2]

(2) Holographic contouring by the Lippman process [Ref. 3]

Typical contour maps produced by each of these techniques are shown in Fig. 15. The contour map in Fig. 15b was produced with the aid of an auxiliary imaging system which is described in the Appendix. This contour map is clearly inferior to that shown in Fig. 15a which was produced by the Lippman process of holography. In this section an investigation to determine the causes of this difference in quality is described. Research to date indicates that chromatic aberrations caused by the auxiliary imaging system is the primary cause of low quality.

This investigation also illustrates the importance of careful optical alignment of multiple-frequency contouring systems which are to be used for making precision measurements. A detailed discussion of the optical alignment procedure is presented in the Appendix.

5.2. ERRORS IN MULTIPLE-FREQUENCY CONTOURING WITH AUXILIARY IMAGING SYSTEMS

The lenses used in this experiment were of a very high quality. They were, however, designed specifically for telescopic imaging at 6328 Å; the specifications were for resolution of better than 100 lines/mm over an object field of roughly 4 cm. These lenses were chosen to determine whether they would produce results comparable to those of the Lippman hologram contouring system.

The initial results of the experiment were almost completely negative; contour fringes were barely visible even at f/100. It was suspected that only strong chromatic effects could cause such a severe deterioration of contour fringe formation. On the other hand, it seemed unlikely that chromatic effects would be significant for a wavelength change as small as the 210 Å encountered in the experiments. However, a simple imaging test showed that the 6328-Å image plane was, in fact, about 2.5 mm away from the 6118-Å image plane. This measurement clearly indicated a possible cause of the poor results. In order to investigate this effect further, the experimental setup described in the Appendix was modified to allow the hologram five degrees of freedom in movement.

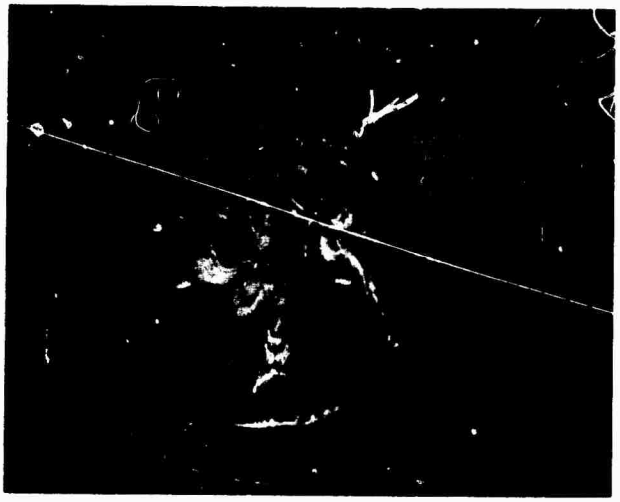

(a) Contours Produced by Lippman Process

(b) Contours Produced with Auxiliary Imaging System

FIGURE 15. COMPARISON OF CONTOUR MAPS

After the usual real-time contouring procedure had been followed, the hologram was moved into the image plane for the real-time wavelength. Due to a misalignment of the translation device, certain undesirable lateral translations had to be corrected before the two images were superimposed. The proper translation along the telescopic axis had been measured roughly as mentioned above. After making this rough adjustment, a trial-and-error search was performed to find the optimum. Since the telescope axis and the corresponding translation table were not perfectly aligned, this search was difficult, and the final position probably could have been better. Nevertheless, the contour map obtained by this procedure (Fig. 16) was considerably better than that shown in Fig. 15b. Since the translational hologram movement made such striking improvements when a highly chromatic telescope was used, it seemed likely that some similar adjustment would improve the results obtained with any telescope. This possibility was tested by repeating the experiment used to obtain Fig. 15b. This time the translation procedure described above was followed.

Before describing the results of this experiment, a further observation should be made about the lenses which were used. The shift in image plane location for different wavelengths is due to the change in lens focal length caused by dispersion. Ideally, the separation of the two lenses which form the telescope should also be changed when the wavelength is changed in order to maintain a unit magnification. This should improve the fringe localization (or image alignment), while simultaneously insuring that depth contours are obtained. This was attempted, but insufficient alignment accuracy produced negative results (i.e., no observable improvement). Another measurement of the chromatic effect was made. This measurement indicated the source of some previously noted, but unexplained, contour fringe errors. Figure 17 shows one of the earliest results obtained with an auxiliary telescope. The curvature of the fringes on the supposedly flat plates behind the coin could not be explained. Curvature is normal since the plates were not optically flat, but it was not clear why the curvature was of the same orientation for all four plates.

One explanation was found by passing a well-collimated beam through the telescope and contouring its wavefront. The usual multiple-frequency contouring technique was followed, except a plane wave was used in place of an object wave. The highly chromatic lenses were used in the telescope. Figure 18 shows a sequence of results obtained using plane waves. In Fig. 18a, the real-time interference of a plane wave at 6118 Å with its holographic reconstruction is shown. The fringes were caused by experimental error and were eliminated by using higher quality optics. In Fig. 18b, the wavelength was changed to 6328 Å, and the reconstruction beam was rotated to minimize the fringe count. Since the reconstruction beam is collimated, the reconstructed wave is collimated. The curvature of the fringes is thus due only to the change in chromatic focal length of the telescope lenses. It is easy to see how this spherical phase error could distort the expected linear fringes into the curved fringes of Fig. 17. By moving one telescope lens a small distance along the optical axis, we were able to reduce

FIGURE 16. IMPROVED CONTOUR MAP PRODUCED WITH APPROPRIATE HOLOGRAM DISPLACEMENT

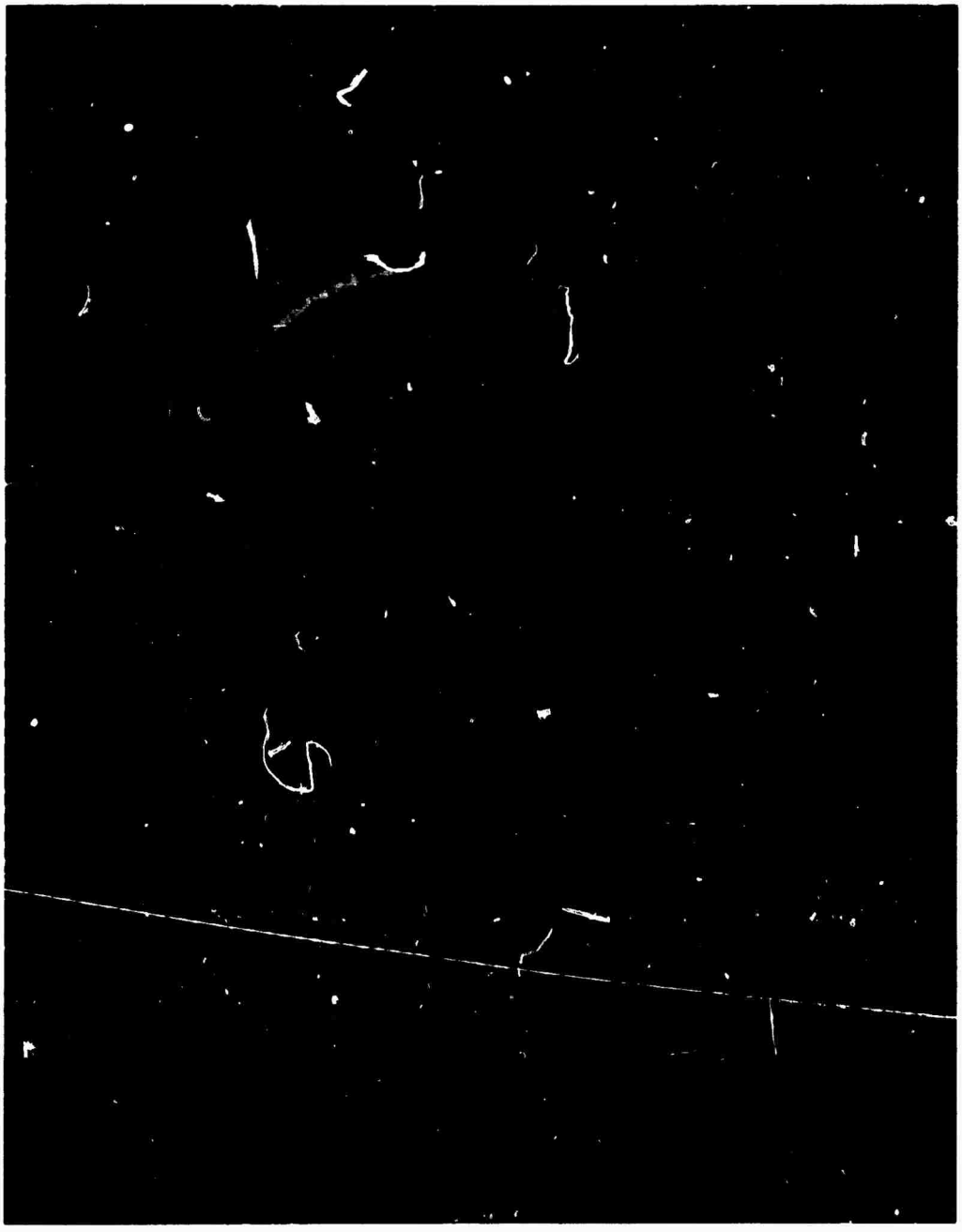

FIGURE 17. CONTOUR MAP WITH FRINGE CURVATURE ERRORS RESULTING FROM CHROMATIC ABERRATIONS

(a) No Change in Wavelength Between Recording and Reconstruction

(b) Fringes After Wavelength Change of 210 Å

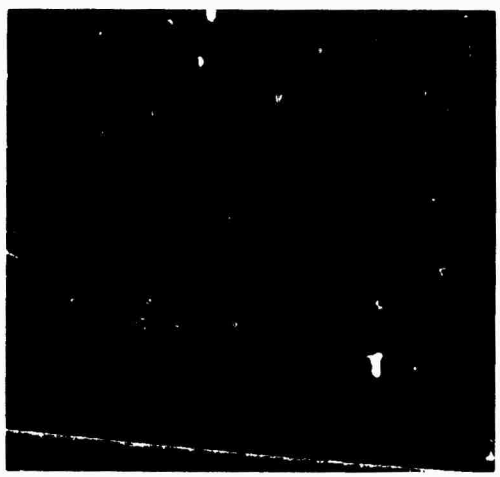

(c) Fringe After Axial Translation of Lens

FIGURE 18. RESULTS OF CHROMATIC ABERRATION EXPERIMENT

the fringe count to the same as that obtained at 6118 Å, (Fig. 18c). The radius of curvature of the telescope output at 6328 Å for a plane wave is given by R:

$$R = \frac{f^2}{2\epsilon}$$

where f is the focal length at 6118 Å, and ϵ is the change in focal length between 6118 Å and 6328 Å. The fringes in Fig. 18b give a measure of this curvature. Considering only the quadratic term of a Taylor series expansion of the spherical wave phase function ϕ, we have

$$\phi = \frac{2\pi}{\lambda}\left(\frac{x^2}{2R}\right)$$

The first zero of the interference would thus be at x_0 where

$$\phi = \pi = \frac{2\pi}{\lambda}\left(\frac{x_0^2}{2R}\right)$$

This yields

$$R = \frac{x_0^2}{\lambda}$$

In the case of Fig. 18b, x_0 is about 1 cm.

$$R = \frac{10^{-4}\ m^2}{0.6 \times 10^{-6}\ m} = 160\ m$$

For these order-of-magnitude calculations, we take f to be 0.5 m. We thus find that

$$\epsilon = \frac{f^2}{2R} = \frac{2500 \times 10^{-4}}{2 \cdot 160} = 0.8\ mm$$

The total axial displacement of the lens which would be required to remove the effect of chromatic aberration is thus $2\epsilon = 1.6$ mm. This is in quite close agreement with the hologram displacement which experimentally improved contour quality.

It is therefore concluded that chromatic aberration is a primary cause of poor quality in multiple-frequency holographic contouring when an auxiliary lens system is used to image the object onto the hologram plane. This effect can be minimized by appropriate axial displacement of the hologram when the wavelength is changed.

6
ABERRATIONS IN ACOUSTICAL HOLOGRAPHY

6.1. INTRODUCTION

One of the primary difficulties in the practical application of acoustical holography has been the presence of aberrations in the optical image. These aberrations reduce the resolution of the holographic imaging system. Various distortions of the image shape also occur. A practical holographic system must not have excessive aberrations. A computer simulation of acoustical holograms was carried out to determine some numerical estimates for the aberrations and to test several techniques for reducing the aberrations by varying the hologram geometry.

This section concerns the aberrations in holographic systems characterized by a ratio of reconstruction wavelength to recording wavelength of the order of 10^{-3}. This discussion is limited to those systems using a plane reference beam and with the hologram scaled by a factor greater than the wavelength ratio. An in-line hologram geometry is examined where the reconstruction beam is placed, such that the image of a selected object point on the optical axis has zero aberrations. The aberrations for off-axis object points are then calculated. For off-axis holograms, a technique for balancing spherical aberration and astigmatism has been modified for application to scaled holograms. Some general rules for the optimum recording geometry are developed. The aberrations for the balanced off-axis system are calculated and compared to those of the in-line system.

6.2. BACKGROUND

Aberrations in holographic imagery have been studied previously by Leith, et al. [12], Meier [13], and Champagne [14]. Aberrations are present in holography when certain well-known geometries are not used in the hologram reconstruction. If the hologram is recorded at one wavelength, λ_o, and reconstructed at another wavelength, λ_c, aberrations may be avoided only if the hologram and the reconstruction geometries are scaled by a scaling factor $m\,\lambda_c/\lambda_o$. The recording of holograms using microwaves and ultrasonic waves is being studied [15, 16]; the wavelength ratios, μ, are typically on the order of 10^{-3}. The recording of acoustical holograms is accomplished through measurements over a range on the order of 1 m. These two conditions present significant problems if the hologram is to be scaled to eliminate aberrations. The scaled hologram will be on the order of 1 mm in diameter.

A partial scaling by a factor of $m > \mu$ is more readily realizable. This is standard procedure for those holographic systems using a scanning detector. The output of the detector is usually recorded on film with a CRT device.

If we are to obtain good imagery using ultrasonic or microwave holography, it is necessary to determine what recording and reconstruction geometries should be used to reduce the aberrations to an acceptable level.* In particular, we would like to discover a technique for finding such an acceptable geometry.

6.3. SYSTEM DESCRIPTION

In our examination of this problem, only plane wave reference beams were used. This simplifies the implementation of an electronically introduced reference beam in scanning-type recording devices. Furthermore, the following values were chosen as typical constants for the numerical calculations [15, 16]:

$$\lambda_c = 6.328 \quad 10^{-7} \text{ m}$$

$$\lambda_o = 3.750 \times 10^{-4} \text{ m}$$

$$\mu = 0.00169$$

Diameter of unscaled hologram = 1.0 m

Scaling factor: m = 0.05

We have chosen Champagne's notation (Fig. 19) and expressions for the Gaussian image points and aberrations [14]. In this notation the position of a point source or image such as point Q in Fig. 19 is specified by R, α, and β. For a plane wave source, we specify only α and β and let R go to infinity in our expressions. The subscript q in Fig. 19 can be any of the following: i = image beam; c = reconstruction beam; o = object beam; r = reference beam.

Champagne obtained his expressions by matching the phase of the reconstruction beam after it had passed through the hologram with that of a hypothetical point image. The phases were expanded in a power series. The first order terms yielded the Gaussian image expressions:

$$\frac{1}{R_i} = \frac{1}{R_C} \pm \frac{\mu}{m^2}\left(\frac{1}{R_o} - \frac{1}{R_r}\right) \tag{13}$$

$$\sin \alpha_i = \sin \alpha_c \pm \frac{\mu}{m}(\sin \alpha_o - \sin \alpha_r) \tag{14}$$

$$\cos \alpha_i \sin \beta_i = \cos \alpha_c \sin \beta_c \pm \frac{\mu}{m}(\cos \alpha_o \sin \beta_o - \cos \alpha_r \sin \beta_r) \tag{15}$$

*We refer to Ref. [17], page 204: "In ordinary instruments, the wave aberrations may be as much as 40 or 50 wavelengths, but in instruments used for more precise work (such as astronomical telescopes or microscopes) they must be reduced to a much smaller value, only a fraction of a wavelength."

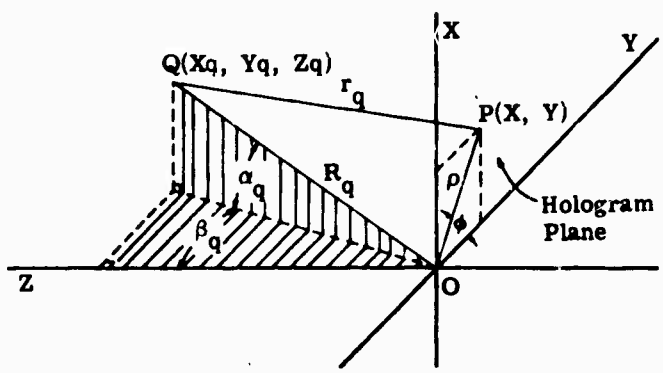

FIGURE 19. COORDINATE GEOMETRY OF AN ARBITRARY POINT SOURCE. Q is at X_q, Y_q, Z_q in form of a hologram in the X, Y plane.

The third-order terms yielded the aberration expression:

Wave aberration = Δ =

$$+\frac{1}{\lambda_c}\Big[-\frac{1}{8}\rho^4 S \qquad \text{spherical aberration}$$

$$+\frac{1}{2}\rho^2(\rho C_x \cos\phi + \rho C_y \sin\phi) \qquad \text{coma} \tag{16}$$

$$-\frac{1}{2}\Big(\rho^2 A_x \cos^2\phi + \rho^2 A_y \sin^2\phi$$

$$2\rho^2 A_{xy} \sin\phi\cos\phi\Big)\Big] \qquad \text{astigmatism}$$

where

$$S = \frac{1}{R_c^3} \pm \frac{\mu}{m^4}\left(\frac{1}{R_o^3} - \frac{1}{R_r^3}\right) - \frac{1}{R_i^3} \tag{17}$$

$$C_x = \frac{\sin\alpha_c}{R_c^2} \pm \frac{\mu}{m^3}\left(\frac{\sin\alpha_o}{R_o^2} - \frac{\sin\alpha_r}{R_r^2}\right) - \frac{\sin\alpha_i}{R_i^2} \tag{18}$$

$$C_y = \frac{\cos\alpha_c \sin\beta_c}{R_c^2} \pm \frac{\mu}{m^3}\left(\frac{\cos\alpha_o \sin\beta_o}{R_o^2} - \frac{\cos\alpha_i \sin\beta_i}{R_r^2}\right) - \frac{\cos\alpha_r \sin\beta_r}{R_i^2} \tag{19}$$

$$A_x = \frac{\sin^2\alpha_c}{R_c} \pm \frac{\mu}{m^2}\left(\frac{\sin^2\alpha_o}{R_o} - \frac{\sin^2\alpha_r}{R_o}\right) - \frac{\sin^2\alpha_i}{R_i} \tag{20}$$

$$A_y = \frac{\cos^2\alpha_c \sin^2\beta_c}{R_c} \pm \frac{\mu}{m^2}\left(\frac{\cos^2\alpha_o \sin^2\beta_o}{R_o} - \frac{\cos^2\alpha_r \sin^2\beta_r}{R_r}\right) - \frac{\cos^2\alpha_i \sin^2\beta_i}{R_i} \tag{21}$$

$$A_{xy} = \frac{\sin\alpha_c \cos\alpha_c \sin\beta_c}{R_c} \pm \frac{\mu}{m^2}\left(\frac{\sin\alpha_o \cos\alpha_o \sin\beta_o}{R_o} - \frac{\sin\alpha_r \cos\alpha_r \sin\beta_r}{R_r}\right)$$

$$- \frac{\sin\alpha_i \cos\alpha_i \sin\beta_i}{R_i} \tag{22}$$

where the upper sign refers to primary image, and the lower sign refers to conjugate image.

6.4. IN-LINE HOLOGRAMS

For an in-line hologram geometry, coma and astigmatism are zero for a point object on the optical axis. To eliminate aberrations completely for a point object on the optical axis, it is a simple matter to set S, the spherical aberration coefficient, equal to zero for a specific recording geometry. Using Eq. (13) for R_i and setting S = 0, we obtain

$$R_c^2\left[\pm\frac{\mu}{m^4}\frac{1}{R_o^3}-\left(\frac{\mu^3}{m}\right)\frac{1}{R_o^3}\right]+R_c\left(\frac{-3\mu^2}{m^4R_o^2}\right)+\left(\frac{\mp 3\mu}{m^2R_o}\right)=0 \qquad (23)$$

The solution of this equation for R_c in terms of μ, m, and R_o gives us the desired reconstruction geometry. For this geometry, the image of a point object on the optical axis at distance R_o from the hologram will be free of aberrations.

In practice, we are usually more concerned with a two- or three-dimensional region than with a single point object. We therefore calculated the aberrations for the images of point objects in the vicinity of our initial object point, keeping the same reference and reconstruction beams. We have plotted the aberrations as a function of α_o in Fig. 20 and as a function of R_o in Fig. 21. The aberrations due to a variation in β_o are identical to those due to a variation in α_o because of the symmetry of the system. As expected, the aberrations increase as the object point is moved away from the aberration-free point. We note that by restricting the size of the object, the maximum aberration can be kept at an acceptable level.

6.5. OFF-AXIS HOLOGRAMS

The presence of aberrations is not the only factor that degrades holographic images. The use of in-line geometry results in the simultaneous presence of light from the primary and conjugate images and undiffracted light. Separation of the desired image can be accomplished by using an off-axis geometry. If the minimum spatial frequency component of the object beam is greater than the spatial frequency of the reference beam, the image beams will be separated. The use of off-axis reference and object beams, however, introduces coma and astigmatism for all points in the object field in the geometry of interest here. We can appreciate the magnitude of this problem by examining the aberrations that result for a point object when the reconstruction beam is a plane wave and is identical to the reference beam. For example, if we have plane wave reference and reconstruction beams at

$$\alpha_r = \alpha_c = 45.0^\circ \qquad \beta_r = \beta_c = 0.0^\circ$$

and a point object at

$$R_o = 0.5 \text{ m} \qquad \alpha_o = 0.0^\circ \qquad \beta_o = 0.0^\circ$$

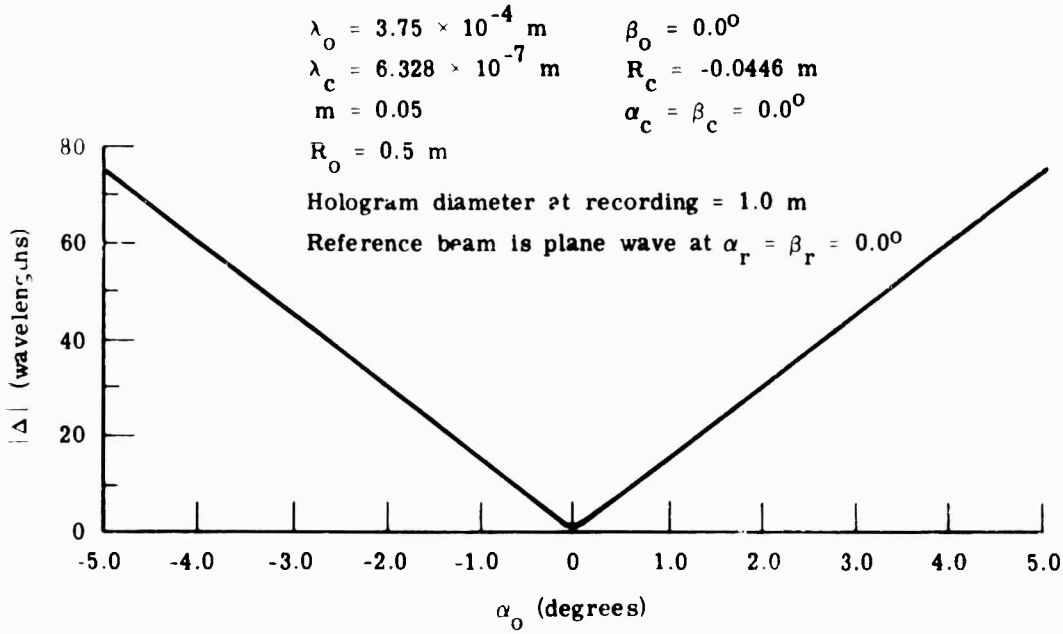

FIGURE 20. MAGNITUDE OF THE WAVE ABERRATION |Δ| VS. α_o

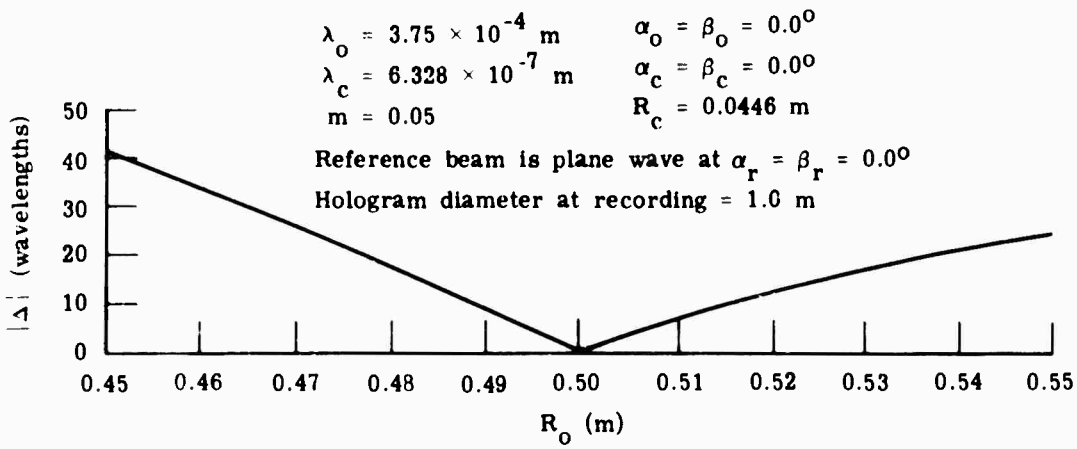

FIGURE 21. MAGNITUDE OF THE WAVE ABERRATION |Δ| VS. R_o

The total wave aberration is .06 λ. If we choose to have the object beam off axis with, for example,

$$R_o = 1.0 \text{ m} \qquad \alpha_o = 45.0^o \qquad \beta_o = 0.0^o$$

and place our plane wave reference and reconstruction beams at

$$\alpha_r = \alpha_c = 0.0^o \qquad \beta_r = \beta_c = 0.0^o$$

the wave aberration is 305 λ. In almost all situations, the aberrations in these examples would be regarded as excessive.

6.6. ABERRATION BALANCING

Significant reduction in aberrations in holograms recorded at one particular wavelength and reconstructed at a different wavelength have been reported when an aberration-balancing technique is used [18]. We will limit the discussion to systems in which $\beta_o = \beta_r = \beta_i = 0$. The aberration-balancing technique first sets the coma coefficient C_x equal to zero. We then set the maximum value of spherical aberration equal to minus the maximum value of astigmatism. The maximum values of spherical aberration and astigmatism occur at $\phi = 90^o$ and $\rho = \rho_{\text{maximum}}$ (Fig. 19). We therefore write

$$C_x = \left[\frac{\sin\alpha_c}{R_c^2} - \frac{\sin\alpha_i}{R_i^2} \pm \frac{\mu}{m^3}\left(\frac{\sin^2\alpha_o}{R_o} - \frac{\sin^2\alpha_r}{R_r}\right)\right] = 0 \tag{24}$$

$$-\frac{1}{8}\rho_{max}^4\left[\frac{1}{R_c^3} - \frac{1}{R_i^3} \pm \frac{\mu}{m^4}\left(\frac{1}{R_o^3} - \frac{1}{R_r^3}\right)\right] = \frac{1}{2}\rho_{max}^2\left[\frac{\sin^2\alpha_c}{R_c} - \frac{\sin^2\alpha_i}{R_i} \pm \frac{\mu}{m^2}\left(\frac{\sin^2\alpha_o}{R_o} - \frac{\sin^2\alpha_r}{R_r}\right)\right] \tag{25}$$

For a given reference beam and point object, we have a set of four equations, (13), (14), (24), and (25), with four unknown variables, R_c, α_c, P_i, and α_i. Solving the equations for α_c and R_c, we obtain

$$\sin\alpha_c = \frac{G + 2FGR_c + GF^2R_c^2 - DR_c^2}{2FR_c - F^2R_c^2} \tag{26}$$

and a fourth-order equation for R_c

$$R_c^4\left(\frac{-\rho_{max}^2}{4}BF^4 + \frac{\rho_{max}^2}{4}F^7 + D^2F - EF^4\right) + R_c^3\left(\frac{7}{4}\rho_{max}^2F^6 - \rho_{max}^2F^3B + 2GF^2D - F^4G^2 - 4EF^3\right)$$
$$+ R_c^2\left(\frac{19}{4}\rho_{max}^2F^5 - \rho_{max}^2BF^2 + 2GFD - 4G^2F^3 - 4EF^2\right)$$
$$+ R_c\left(6\rho_{max}^2F^4 - 6G^2F^2\right) + \left(3\rho_{max}^2F^3 - 3G^2F\right) = 0 \qquad (27)$$

where $B = \pm\frac{\mu}{m^4}\left(\frac{1}{R_o^3} - \frac{1}{R_r^3}\right)$

$$D = \pm\frac{\mu}{m^3}\left(\frac{\sin\alpha_o}{R_o^2} - \frac{\sin\alpha_r}{R_r^2}\right)$$

$$E = \pm\frac{\mu}{m^2}\left(\frac{\sin^2\alpha_o}{R_o} - \frac{\sin^2\alpha_r}{R_o}\right)$$

$$F = \pm\frac{\mu}{m^2}\left(\frac{1}{R_o} - \frac{1}{R_r}\right)$$

$$G = \pm\frac{\mu}{m}(\sin\alpha_o - \sin\alpha_r)$$

where the +(-) sign is for the primary (conjugate) image. We will solve Eq. (27) for R_c numerically.

This method differs from the previously reported work [18] since the hologram scaling factor has been included in the calculations. Furthermore, the variables in the recording geometry are the independent variables rather than the dependent variables. This permits us to restrict the recording geometry to within the bounds set by the equipment. In particular, the reference beam can be restricted to be only a plane wave. In addition, once the reconstruction geometry has been determined by Eqs. (26) and (27) for a specific object point, which we will term the compensated point, the aberrations for the images of point objects near the compensated point can be readily examined.

From Eq. (16) we see that while spherical aberration varies as the fourth power of the hologram coordinate, astigmatism varies as the second power. We also note that while spherical aberration is independent of ϕ, astigmatism varies as $\cos^2\phi$ (assuming that $\beta_o = \beta_r = \beta_c$

$\beta_i = 0.0^o$). It is therefore evident that the aberration-balancing technique as described by Eqs. (24) and (25) will not eliminate the aberrations over the hologram surface but will merely reduce them. We would expect that the degree of reduction of the aberrations will be a function of the recording geometry variables, which are the independent variables of Eqs. (26) and (27). We will examine this functional dependence by independently varying α_r and α_o. We define $|\Delta_{max}|$ as the maximum deviation of the actual wavefront from the Gaussian sphere wavefront over the hologram surface. We will use $|\Delta_{max}|$ as a measure of the aberrations.

We first arbitrarily set $\alpha_r = 45.0^o$, and $R_o = 0.5$ m. We then vary α_o. For each value of α_o, the reconstruction geometry is determined by Eq. (26) and (27). The value of $|\Delta_{max}|$ for the compensated point, a function of α_o, is plotted in Fig. 22. We see that as $|\alpha_o|$ increases, $|\Delta_{max}|$ decreases. Separation of the primary and conjugate images will occur for $\alpha_o < 0.0^o$. We can also set $\alpha_o = -45.0^o$, and $R_o = 0.5$ m, and vary α_r. For each value of α_r, the reconstruction geometry is determined by Eqs. (26) and (27). The value of $|\Delta_{max}|$ for the compensated point, $\alpha_o = -45.0^o$ and $R_o = 0.5$ m, is plotted as a function of α_r in Fig. 23. We see that as α_r decreases, $|\Delta_{max}|$ decreases. Separation of the primary and conjugate images occurs for $\alpha_r < 27.5^o$.

We naturally want the smallest possible value of $|\Delta_{max}|$. We therefore attempt to combine the two effects noted by selecting a large value for $|\alpha_o|$ and small value for $|\alpha_r|$:

$$\alpha_o = 75.0^o \qquad R_o = 0.5 \text{ m} \qquad \alpha_r = -10.0^o$$

The reconstruction geometry and conjugate image location are determined by Eqs. (26), (27), (13), and (14) to be

$$R_c = -0.0448 \text{ m} \qquad \alpha_c = -29.59^o \qquad R_i = -0.0423 \text{ m} \qquad \alpha_i = -32.16^o$$

For the compensated point, $|\Delta_{max}| = 2.0\ \lambda$. This is a significant reduction in aberrations. As we will seldom want to image a point object, we must examine the aberrations for the images of object points near the compensated point. For these points, coma will not be zero, and the effectiveness of balancing spherical aberration and astigmatism will be decreased. It is necessary to examine the aberrations for these points. Using the reference and reconstruction beams in the last example, the object beam was varied about the compensated point and the aberrations calculated. The value of $|\Delta_{max}|$ is plotted as a function of R_o, α_o, and β_o in Figs. 24, 25, and 26, respectively.

Comparing the aberrations of the in-line geometry (Figs. 20 and 21) to the aberrations of the off-axis geometry (Figs. 24, 25, and 26), we see that in the lateral directions away from the compensated point, the aberrations increase at a much slower rate for the off-axis geometry. The depth of field is, however, greatly reduced for the off-axis geometry. This would not be a problem if plane-to-plane imaging is desired.

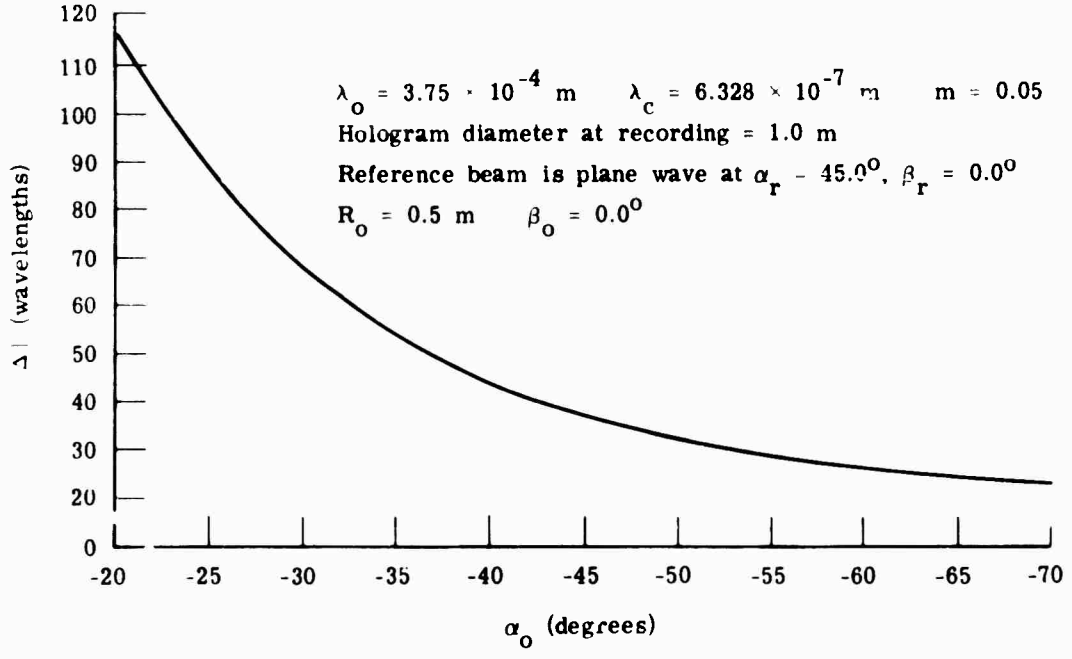

FIGURE 22. MAGNITUDE OF THE WAVE ABERRATION $|\Delta|$ FOR THE COMPENSATED OBJECT POINT VS. α_o. For each value of α_o, the reconstruction geometry is calculated according to the aberration-balancing technique. The wave aberration is then calculated using the new values of α_o, R_c, and α_c.

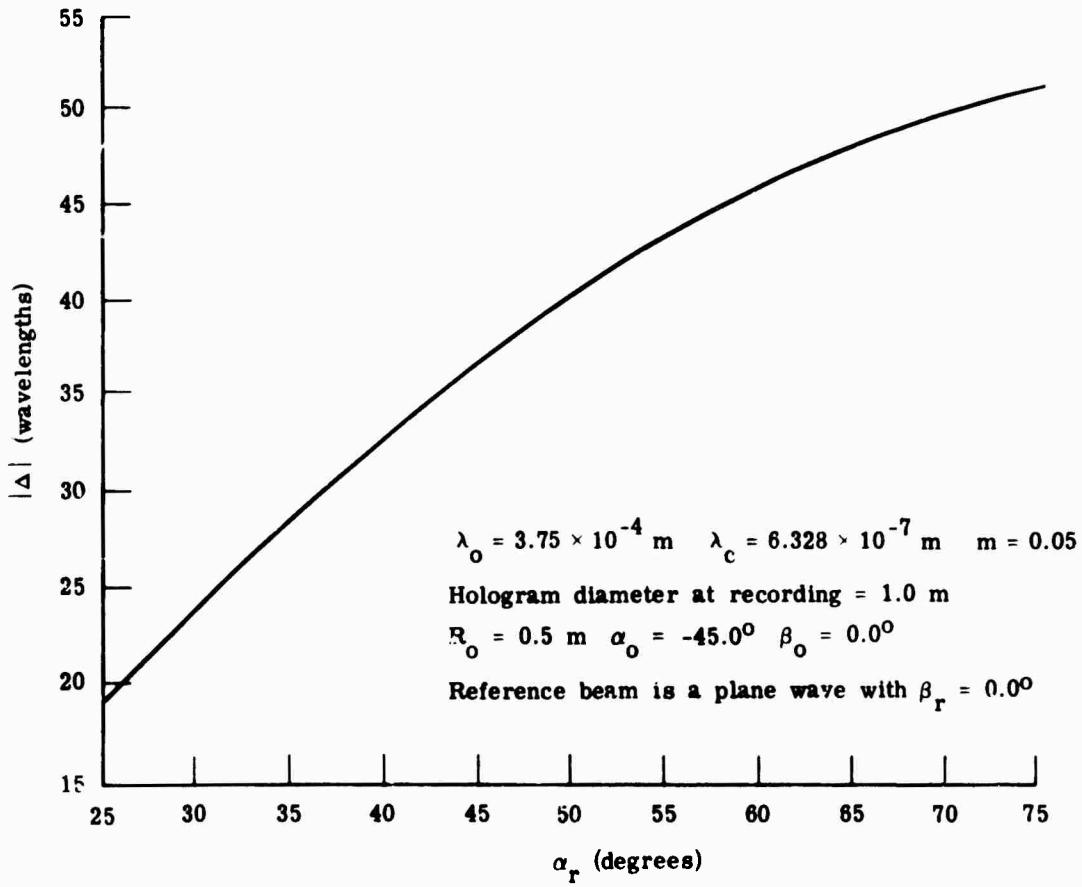

FIGURE 23. MAGNITUDE OF THE WAVE ABERRATION $|\Delta|$ FOR THE COMPENSATED OBJECT POINT VS. α_r. For each value of α_r, the reconstruction geometry is calculated according to the aberration-balancing technique. The wave aberration is then calculated using the new values of α_r, R_c, and α_c.

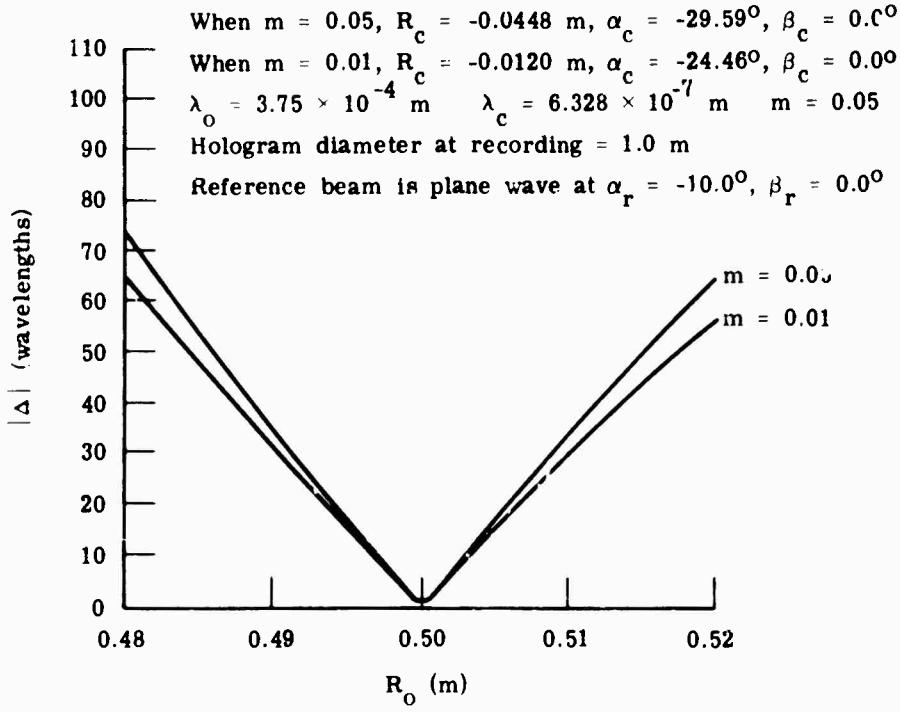

FIGURE 24. MAGNITUDE OF THE WAVE ABERRATION $|\Delta|$ VS. R_o USING ABERRATION BALANCING. The reconstruction geometry is calculated for the object point, R_o = 0.5 m, α_o = 75.0°, β_o = 0.0°, according to the aberration-balancing technique. For each value of m, R_c and α_c, the wave aberration is calculated as a function of R_o, with α_o = 75.0° and β_o = 0.0°.

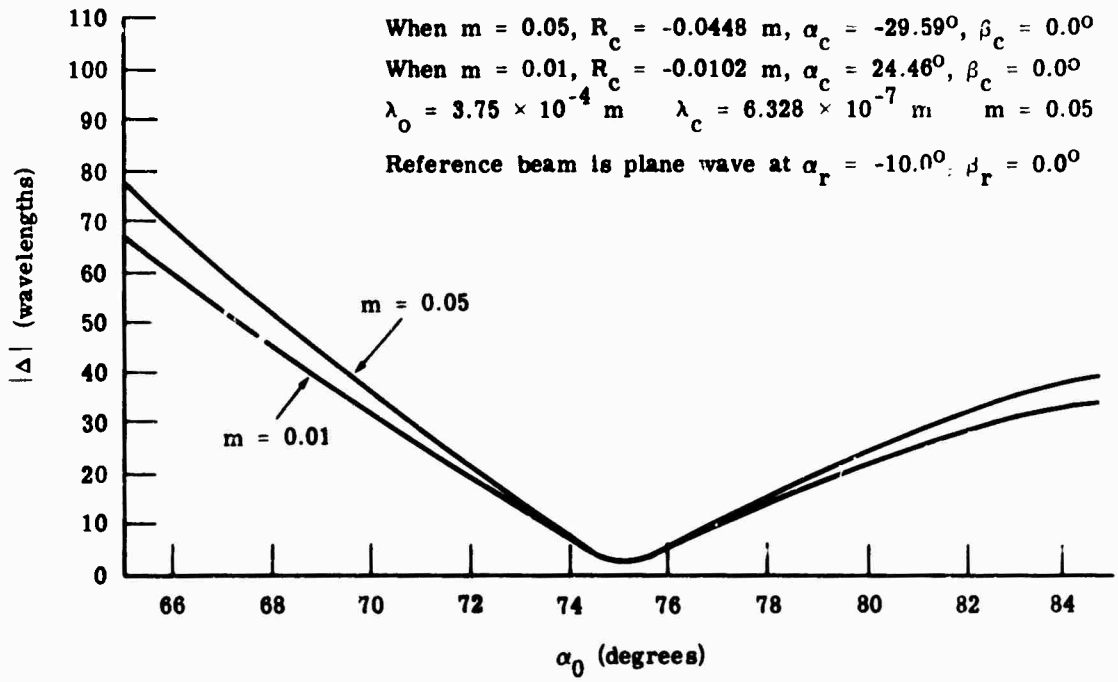

FIGURE 25. MAGNITUDE OF THE WAVE ABERRATION |Δ| VS. α_o USING ABERRATION BALANCING. The reconstruction geometry is calculated for the object point R_r = 0.5 m, α_o = 75.0°, β_o = 0.0°, according to the aberration-balancing technique. For each value of m, R_c and α_c, the wave aberration is calculated as a function of α_o, with R_o = 0.5 m, and β_o = 0.0°.

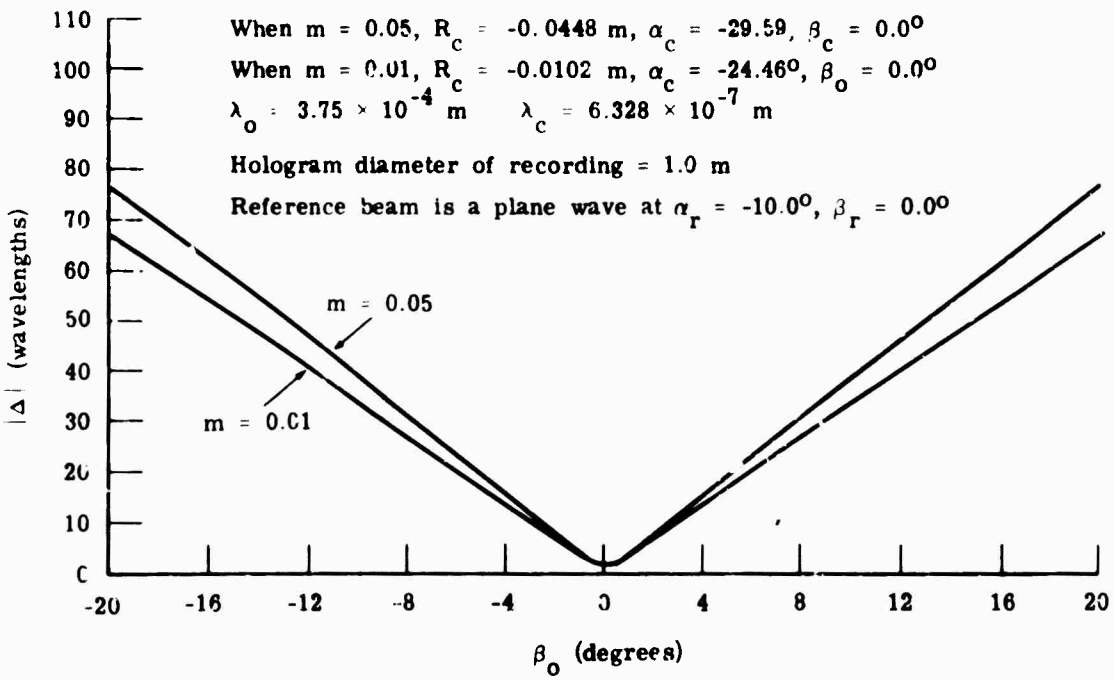

FIGURE 26. MAGNITUDE OF THE WAVE ABERRATION |Δ| VS. β_o USING ABERRATION BALANCING. The reconstruction geometry is calculated for the object point R_o = 0.5 m, α_o = 75.0°, β_o = 0.0°, according to the aberration-balancing technique. For each value of m, R_c and α_c, the wave aberration is calculated as a function of β_o, with R_o = 0.5 m, and α_o = 75.0°.

It is important to note that for the off-axis hologram, the lateral magnification in the α direction varies from 0.6×10^{-3} at $\alpha_o = 80^o$ to 1.2×10^{-3} at $\alpha_o = 70^o$. The longitudinal magnification remains constant to the indicated accuracy at 2.8×10^{-3}. The large variation in the lateral magnification, indicative of significant distortion, is due to the large value of α_o. By decreasing α_o, we can reduce this variation in lateral magnification, but at the same time we reduce the effectiveness of the aberration-balancing technique. We examine this problem by choosing for our compensated point $R_o = 0.5$ m and $\alpha_o = 45.0^o$ and by setting $\alpha_r = -25.0^o$ for proper image separation. The reconstruction beam is given by Eqs. (26) and (27) as $R_c = -0.0469$ m and $\alpha_c = -18.24^o$. Figures 27, 28, and 29 show the aberrations, $|\Delta_{max}|$, for object points near the compensated point. The lateral magnification in the α direction varies from 2.4×10^{-3} at $\alpha_o = 40^o$ to 2.0×10^{-3} at $\alpha_o = 50^o$. The variation in lateral magnification has decreased although $|\Delta_{max}|$ has increased by approximately 16 λ. For comparison, the lateral magnification for the in-line hologram was virtually constant at 2.8×10^{-3}.

We initially set the hologram scaling factor m at 0.05. This was arbitrary since most CRT film recorders can be used with various scaling factors. It therefore seemed reasonable to question the choice of $m = 0.05$. We found, however, that there was negligible change in the aberrations as m was varied until it was within a factor of 2 or 3 of μ. In Figs. 23, 24, and 25, we have superimposed the aberrations for a system with the same recording geometry, but with $m = 0.01$. These curves reveal a very small change in $|\Delta_{max}|$. As m approaches μ, the aberrations for all object points go to zero. In all geometries that we tried, the aberration-balancing technique provides the aberration free-geometry, if one exists.

6.7. CONCLUSIONS

We have seen that the use of an aberration-balancing technique greatly reduces aberrations in off-axis acoustical holograms. Variations in lateral magnification as a function of α_o indicate the presence of significant distortions. These can be reduced at the expense of increased aberrations. If large objects are to be imaged, an explicit calculation of the distortion and curvature of field will be necessary in order to analyze the image quality. It appears that off-axis holograms will be most useful for the examination of small objects. The large amount of calculations, specifically for the aberration balancing, were accomplished relatively easily with the aid of a digital computer.

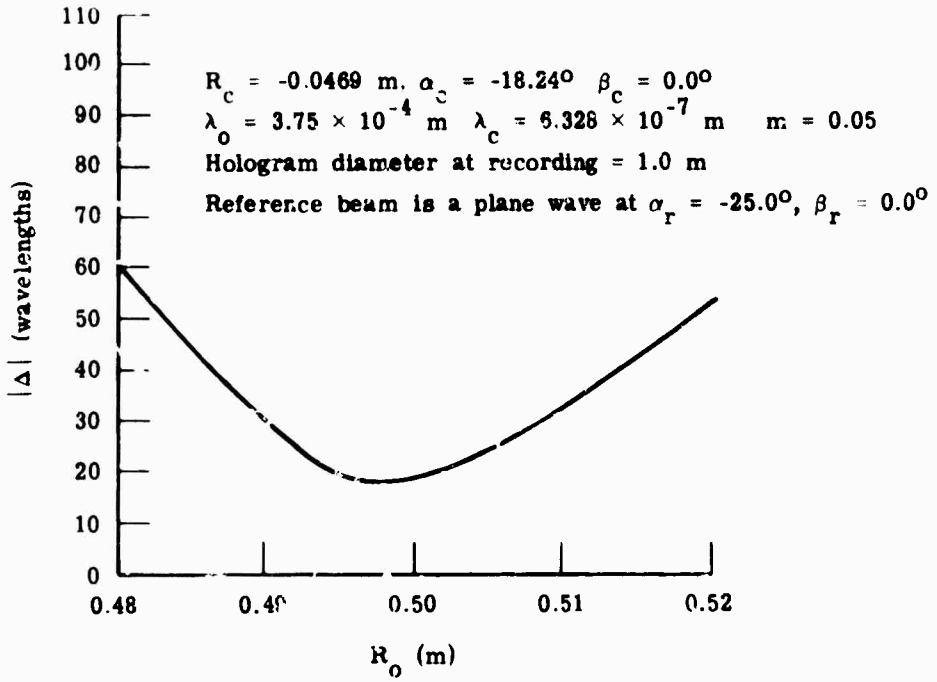

FIGURE 27. MAGNITUDE OF THE WAVE ABERRATION $|\Delta|$ VS. R_o WITH THE OBJECT POINT NEAR THE COMPENSATED POINT. The reconstruction geometry is calculated for the object point $R_o = 0.5$ m, $\alpha_o = 45.0^o$, $\beta_o = 0.0^o$, according to the aberration-balancing technique. The wave aberration is calculated as a function of R_o, with $\alpha_o = 45.0^o$ and $\beta_o = 0.0^o$.

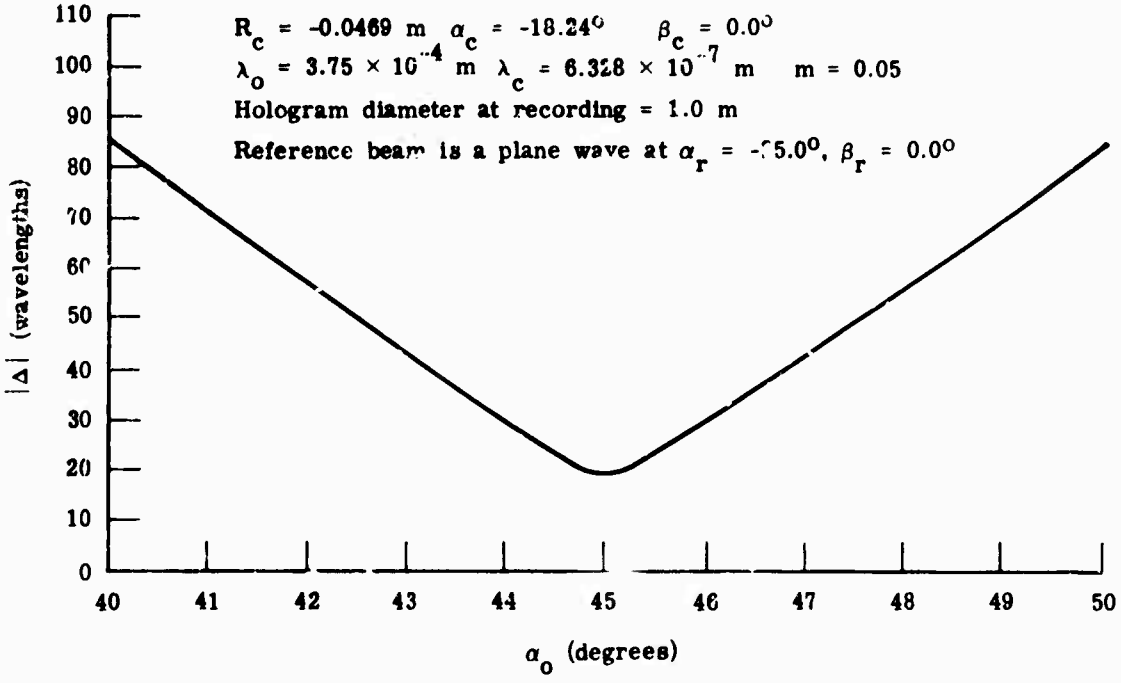

FIGURE 28. MAGNITUDE OF THE WAVE ABERRATION $|\Delta|$ VS. α_o WITH THE OBJECT POINT NEAR THE COMPENSATED POINT. The reconstruction geometry is calculated for the object point R_o = 0.5 m, α_o = 45.0°, β_o = 0.0°, according to the aberration-balancing technique. The wave aberration is calculated as a function of α_o, with R_o = 0.5 m, and β_o = 0.0°.

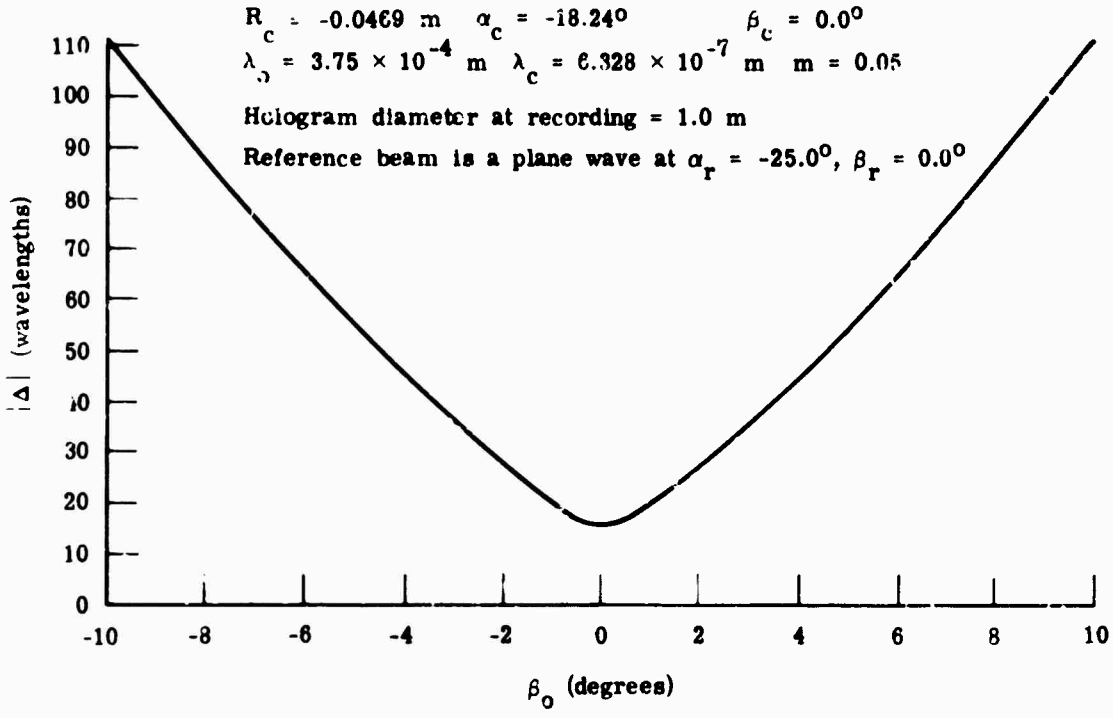

FIGURE 29. MAGNITUDE OF THE WAVE ABERRATION |Δ| VS. β_o WITH THE OBJECT POINT NEAR THE COMPENSATED POINT. The reconstruction geometry is calculated for the object point R_o = 0.5 m, α_o = 45.0°, β_o = 0.0°, according to the aberration-balancing technique. The wave aberration is calculated as a function of α_o with R_o = 0.5 m, and α_o = 45.0°.

APPENDIX
ALIGNMENT PROCEDURES USED FOR MULTIPLE-FREQUENCY HOLOGRAPHIC CONTOURING WITH AN AUXILIARY TELESCOPE

A.1. INTRODUCTION

This appendix describes in detail the alignment procedures used in setting up the major experiments performed. The first objective of alignment is to obtain interference fringes containing depth information about the object. The second objective is to force the contouring surfaces to within certain error bounds of the desired set of contouring surfaces. Most of the work described here was performed to obtain plane contouring surfaces parallel to the hologram surface. The first task is to obtain a well-collimated beam.

A.2. EXPANDING AND COLLIMATING A LASER BEAM

The two techniques used in the experiments to verify the collimation of the beams were autocollimation and wedge interference. These techniques were equally accurate when carefully performed, but the wedge interference method was quicker and more convenient. Both will be described after a brief discussion of the optimum collimation to be expected from typical lasers and optics.

According to Innes and Bloom [19], the minimum spot size from any source must, by reciprocity, be physically realizable itself as a source of light which has a radiation pattern similar to that of a focused beam. Further, they assert that the smallest such source is an "electromagnetic dipole whose radiation pattern is characterized as follows:"

$$E_x = K \cos\theta \quad 0 \leq \theta \leq 180^\circ \tag{28}$$

where K is an arbitrary constant, E_x is the transverse electric field, and θ is measured from the optic axis." Their calculations from such a radiation pattern indicate a minimum spot size of roughly 1 λ in diameter. It is interesting to note that an f/1 optical system can realize this minimum for a Gaussian laser beam. Correspondingly, Innes and Bloom's calculations indicate that smaller f-number optical systems could not reduce the spot size; also, at f/1 the effective source is spherical for Gaussian laser beams. The inherent finiteness of the source will preclude perfect collimation. A simple way of showing this is to use the thin lens equation

$$\frac{1}{d_1} + \frac{1}{d_2} = \frac{1}{f} \tag{29}$$

where d_1 is the distance of the source from the lens, d_2 is the distance of its image from the lens, and f is the focal length of the lens. Since the source is finite, d_1 takes on a range of

values so that d_2 can be infinite (corresponding to a collimated beam) for only one point of the source. We can, however, calculate a value d_{2min} for some arbitrary fraction of the light.

We assume that the central point of the source is at the focal point of the lens so that Eq. (29) becomes

$$\frac{1}{f \pm \epsilon} + \frac{d}{d_2} = \frac{1}{f} \tag{30}$$

where ϵ is the radius of the effective source. We thus find that

$$|d_{2min}| = \frac{2f^2}{\lambda} \tag{31}$$

where ϵ has been set equal to $\lambda/2$. For source points off the lens axis, the light will also diverge even when collimated. A spherical wave of aperture $A = 2x_{max}$ and radius $R(\epsilon)$ would have a corresponding maximum spatial frequency at the lens plane if

$$w_{max} = \frac{x_{max}}{\lambda R(\epsilon)} = \frac{\epsilon}{f\lambda} = \frac{1}{2f} \tag{32}$$

or

$$R\left(\frac{\lambda}{2}\right) = \frac{2fx_{max}}{\lambda}$$

Taking the ratio of Eq. (32) to (31), we have

$$\frac{R\left(\frac{\lambda}{2}\right)}{d_{2min}} = \frac{\lambda}{2f^2}\,\frac{2fx_{max}}{\lambda} = \frac{x_{max}}{f} = \frac{F}{2} \tag{33}$$

so that F = 1/2 appears to be an approximate breakpoint in the relative importance of lateral and longitudinal source dimensions.

A typical example might be to use a collimating lens with the following specifications:

$f = 24$ in.

$F = 4$

$2x_{max} = 6$ in.

$\lambda = 0.63\ \mu m$

and to use an f/1 microscope objective to form the source. We would then have:

$$|d_{2min}| = \frac{2f^2}{\lambda} = \frac{2\left(\frac{24}{40}\right)^2}{0.63 \times 10^{-6}} = 1.16 \times 10^6\ m$$

$$R\left(\frac{\lambda}{2}\right) = \frac{2fx_{max}}{\lambda} \cong \frac{0.5 \times 0.15}{0.6 \times 10^{-6}} \sim 1.2 \times 10^{5}$$

Obviously, the lateral size of the effective source is critical in this example. If the laser beam is not Gaussian due to multimodes or simple optics noise, the corresponding lateral spread in the effective source could easily reduce $R(\epsilon)$ by another order of magnitude.

A.3. ERRORS DUE TO AN UNCOLLIMATED OBJECT ILLUMINATION

The error phase distribution across the object for uncollimated illumination is given approximately by

$$\phi = \left(\frac{2\pi}{\lambda_{eq}}\right)\left(\frac{x^2}{2R}\right) \tag{34}$$

where R is the radius of curvature of the illumination, x is the lateral coordinate of the plane object, and λ_{eq} equals $\lambda_1\lambda_2/2|\Delta\lambda|$. If we require that the phase error be less than $\pi/4$, we have the condition

$$x \cong \sqrt{\frac{\lambda_{eq} R}{4}} \tag{35}$$

This condition can be rewritten

$$\frac{x}{\sqrt{R}} \leq \sqrt{\frac{\lambda_{eq}}{4}} \tag{36}$$

Below is another example. For

$x_{max} = 2$ cm

$\lambda_{eq} = 10\ \mu m$

we find

$$R \geq \frac{4.4 \times 10^{8}}{\lambda_{eq}} = \frac{16 \times 10^{8}\ \mu m}{10}$$

$$R \geq 1.6 \times 10^{2}\ m$$

The above example, relative to the first example, certainly indicates that collimation errors should not be serious. But neither example considered chromatic or other aberrations of the lenses.

A.4. A SEQUENTIAL OUTLINE OF SETUP PROCEDURES

One of the first requirements for an accurate alignment of a holographic measuring system, such as multiple-frequency holographic contouring, is to direct the laser beam parallel to and at a convenient height from the surface of the optical table. A convenient height is generally determined by the height at which the large optical elements can easily be mounted. Once the laser beam is positioned at a convenient height, the beam is directed through a skeleton of the desired setup. This procedure is diagrammed in Fig. 30. The skeleton setup is shown in Fig. 30a.

The first objective is to have the reference and object beam arms of the interferometer either equal in length or at least coherent at the hologram plane. Most lasers can be operated single mode, so that coherence length adjustments may be unnecessary. Next, the object is reflected at 45° by a beam splitter and is incident normal to the object-mounting mirror. Care is taken at all times to keep the laser beam at the chosen height above the working surface. The reflected beam from the object mirror then is incident onto a mirror in the approximate position of the hologram plane. This mirror is rotated until normal incidence is obtained. The alignment plate shown can be used to line up the many reflections obtained when the hologram mirror and the object mirror are parallel and normal to the object illumination mirror. Up to this point, the procedure is generally quite precise.

The steps shown in Fig. 30b are considerably more difficult to accomplish with great precision. The problem is to insert the lenses with their optical axes coincident with the laser beam and in the correct position to perform their function. Variable apertures are placed in the beam at several locations to record its position before any lenses are inserted. The apertures are then closed until they just pass the laser beam. Collimating lenses L_1 and L_2 are placed in the beam at the approximate positions shown. The placement of these lenses is aided by multiple reflections from their surfaces in combination with the alignment apertures. The lens-pinhole devices (temporarily without the pinholes) are then placed in approximate position. The lens pinhole devices should have a mechanism for precise translation lateral and parallel to the laser beam. The devices are moved parallel to the laser beam until collimated beams are obtained; the collimation techniques are described later. Once collimation occurs, apertures A_2 and A_4 (which were open during collimation procedures) are closed down again. If the beams which passed by A_2 and A_4 do not pass through A_3 and A_5, respectively, then lateral adjustment of the lens-pinhole devices will allow the necessary corrections to be made. The pinholes are then positioned at the focal points of the microscope objectives to filter out as much noise as possible without showing diffraction effects. All that remains now is to insert L_3 and then L_4; the lenses L_3 and L_4 shown here are of equal focal length f and are separated by 2f which gives unity magnification. The aperture of the objective lens L_3 must be large enough to gather the desired cones of light from all object points; a rule of

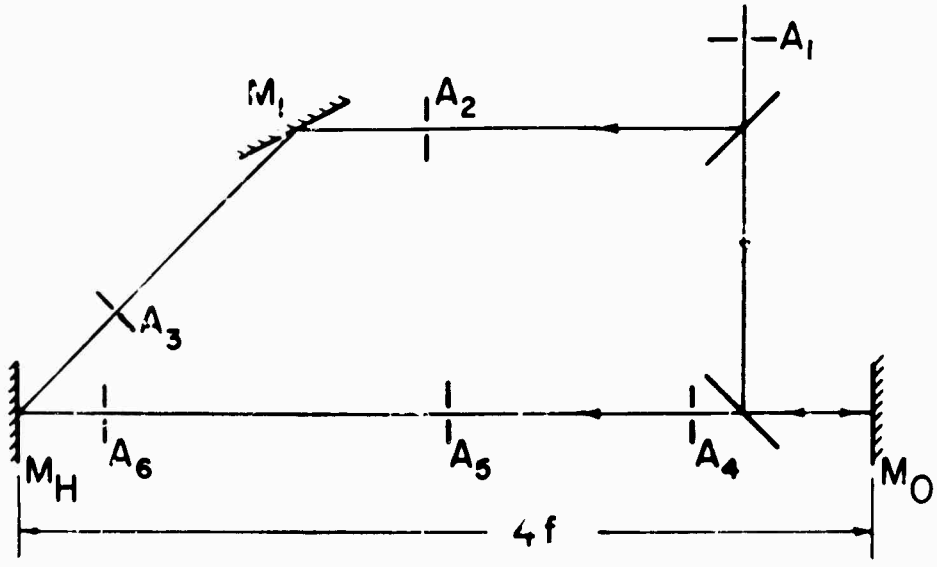

(a) Basic Beam Alignment

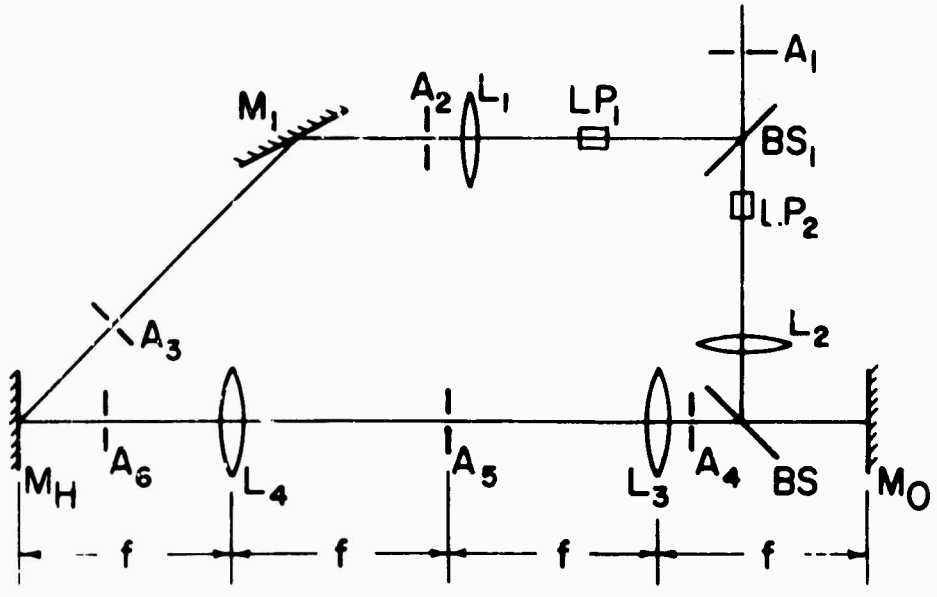

(b) Insertion of Optical Elements

FIGURE 30. SCHEMATIC DIAGRAMS OF ALIGNMENT PROCEDURE

thumb is that the useful aperture of L_3 should be about twice the diameter of the object. First L_4 is placed in position and centered, and A_5 and A_6 are opened. Then L_3 is placed in the beam and adjusted while shifting A_5 to obtain autocollimation from L_4, the hologram mirror, and A_5.

Finally, the object is mounted with known orientation in respect to the object mirror, and the hologram plane is moved more exactly into the image plane of the telescope. In some cases, the accurate orientation of a diffuse object can be an extremely difficult task. An optional adjustment is to remove the beam splitter and illuminate the object from off axis. This will require some form of angular adjustment for the two different wavelengths if depth contour surfaces normal to the optical axis are desired. The advantages are that the object illumination is brighter, and the aberrating effects of the beamsplitter are eliminated.

A.5. AUTOCOLLIMATION

Perhaps the most commonly used check of beam collimation is autocollimation. The expanded beam to be collimated is reflected back upon itself, and the lens-pinhole assembly is moved until the reflected energy passes back through the pinhole. Finer adjustments can be made by maximizing a portion of the light energy reflected back through the pinhole if such energy is available. Another good adjustment is to deflect the reflected spot slightly off the pinhole and maximize the speckle size in the scattered light. When the energy-measuring adjustment is used, accuracy is a function of the pinhole diameter and thickness. For the typical 10-μm in diameter pinhole and f/4 collimating lens, the pinhole can be located to within about 20 μm.

A.6. WEDGE INTERFEROMETER TECHNIQUES

The wedge interferometer concept is illustrated in Fig. 31a. A point source illuminates a wedged beamsplitter, and an interference pattern is observed in plane P. For simplicity, we assume that the beamsplitter uses two virtual point sources which are separated by a distance dependent on θ, $\Delta\theta$, t, and R as defined in Fig. 31a. Since R is very large when the interference fringes become visible to the eye, we will ignore the aberrations on one of the wavefronts leaving the beamsplitter. The coordinate system and the experiment are arranged to keep the first surface virtual image at (o, z). The location of the second surface virtual image is taken to be at $(\Delta x, z + \Delta z)$ where $\Delta x(\theta, \Delta\theta, t, R)$ and $\Delta z(\theta, \Delta\theta, z, R)$ are nontrivial functions. For the moment, we ignore the functional form of these quantities and simply express the fringe pattern in terms of Δx and Δz.

The phase difference ($\Delta\phi$) in plane P can be written

$$\Delta\phi = \frac{2\pi}{\lambda}\left[\sqrt{x^2 + z^2} - \sqrt{(x - \Delta x)^2 + (z + \Delta z)^2}\right] \tag{37}$$

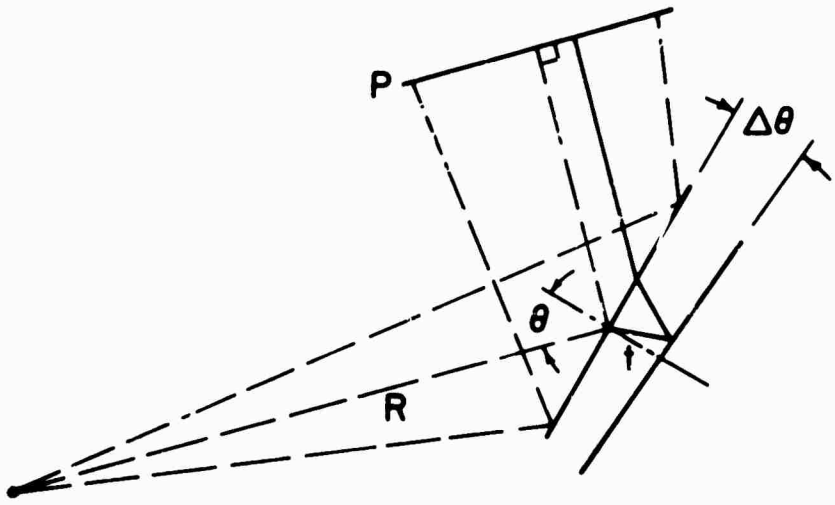

(a) Wedge Interferometer

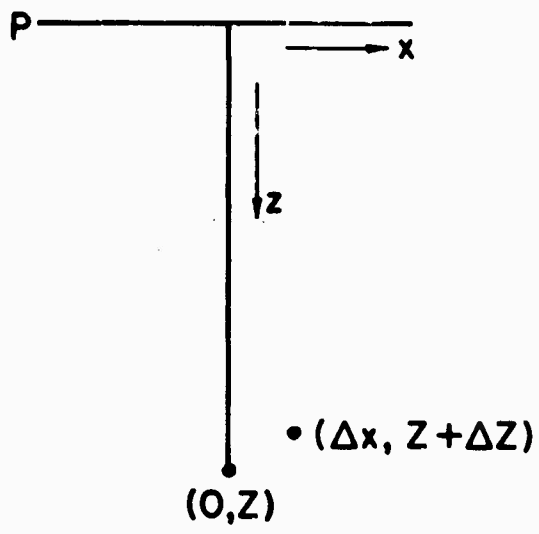

(b) Coordinate System

FIGURE 31. CONFIGURATION FOR WEDGE INTERFEROMETER TECHNIQUES

Making use both of the fact that z/x is considerably greater than unity and of the usual Taylor series expansion of the square roots, we have

$$\Delta\varphi = \left(\frac{2\pi}{\lambda}\right)\frac{-2z\,\Delta z - (\Delta z)^2 - (\Delta x)^2 + 2x\,\Delta x}{2z}$$

For simplicity and at no conceptual loss, we consider the fringes for an area symmetric about the origin, i.e., the area is bounded by $-x_M$ and $+x_M$. The total fringe count is

$$N = \frac{\Delta\phi(x_M) - \Delta\phi(-x_M)}{2\pi} \tag{38}$$

$$= \left(\frac{1}{\lambda}\right)\frac{2x_M\,\Delta x}{z}$$

We can approximate the quantity Δx by

$$\Delta x = \Delta x(t, \theta) - \Delta\theta \cdot R$$

This yields

$$N = \left(\frac{1}{\lambda z}\right)\left|2x_M[\Delta x(t, \theta) - \Delta\theta \cdot R]\right| \tag{39}$$

Obviously N depends on the sign of $\Delta\theta$. As z becomes infinite, however,

$$N \to \left|\frac{2x_M R\,\Delta\theta}{\lambda z}\right| \tag{40}$$

We thus see that the limiting value of N is independent of the sign of the wedge angle. In other words, the fringe count should be independent of a 180° rotation of the beamsplitter. Typically, the accuracy of a fringe count change is to within one fringe. This corresponds to a minimum radius of curvature given by the following relation:

$$\Delta\phi = \frac{\pi}{4} = \left(\frac{2\pi}{\lambda}\right)\frac{x_M^2}{2R_{MIN}} \tag{41a}$$

or

$$R_{MIN} = \frac{4x_M^2}{\lambda} \tag{41b}$$

If $x_M = 7$ cm, and $\lambda = 0.6\ \mu$m, we find

$$R_{MIN} = \frac{40 \times 10^{-4}}{36 \times 10^{-7}} \cong 5 \times 10^3 \text{ m}$$

For the autocollimation techniques, we estimated

$$R_{MIN} = \frac{f^2}{\lambda} = \frac{25 \times 10^{-2}}{25 \times 10^{-6}} \sim 10^4 \text{ m}$$

REFERENCES

1. E. N. Leith et al., Investigation of Holographic Testing Techniques, Report No. 2420-5-P, Willow Run Laboratories of the Institute of Science and Technology, The University of Michigan, Ann Arbor, August 1969.
2. E. N. Leith et al., Investigation of Holographic Testing Techniques Report No. 2420-9-P, Willow Run Laboratories of the Institute of Science and Technology, The University of Michigan, Ann Arbor, April 1970.
3. E. N. Leith et al., Investigation of Holographic Testing Techniques, Report No. 2420-12-P, Willow Run Laboratories of the Institute of Science and Technology, The University of Michigan, Ann Arbor, September 1970.
4. J. M. Burch et al., Dual- and Multiple-Beam Interferometry by Wavefront Reconstruction, Nature, Vol. 209, 1966, p. 1015.
5. K. Biederman, Attempts to Increase the Holographic Exposure Index of Photographic Materials, Appl. Opt., Vol. 9, December 1970.
6. J. W. Goodman et al., Wavefront Reconstruction Imaging through Random Media, Appl. Phys. Letters, Vol. 8, June 1966, p. 311.
7. J. W. Goodman et al., Experiments in Long Distance Holographic Imagery, Appl. Opt., Vol. 8, August 1969, p. 1581.
8. O. Bryngdahl and A. Lohmann, Holographic Penetration of an Inhomogeneous Medium, J. Opt. Soc. Am., Vol. 59, September 1969, p. 1245.
9. E. Leith et al., Holographic Data Storage in Three-Dimensional Media, Appl. Opt., Vol. 5, August 1969, p. 1303.
10. J. W. Goodman, Introduction to Fourier Optics, McGraw-Hill, 1968, pp. 57-62.
11. A. Papoulis, Probability, Random Variables, and Stochastic Processes, McGraw-Hill, 1965, pp. 476-477.
12. E. N. Leith, J. Upatnieks, and K. A. Haines, Microscopy by Wavefront Reconstruction, J. Opt. Soc. Am., Vol. 55, 1965, p. 981.
13. R. W. Meier, Magnification and Third-Order Aberrations in Holography, J. Opt. Soc. Am., Vol. 55, 1965, p. 987.
14. E. B. Champagne, Nonparaxial Imaging, Magnification, and Aberration Properties in Holography, J. Opt. Soc. Am., Vol. 57, 1967, p. 51 (also, A Qualitative and Quantitative Study of Holographic Imaging, Ph.D. Thesis, Ohio State University, Columbus, Ohio, July 1967).
15. A. F. Metherell, H. M. A. El-Sum, and L. Larmore, Acoustical Holography, Vol. 1, Plenum Press, 1969.
16. A. F. Metherell and L. Larmore, Acoustical Holography, Vol. 2, Plenum Press, 1970.
17. M. Born and E. Wolf, Principles of Optics, 3rd Ed., Pergamon Press, 1958.
18. J. N. Latta, Computer-Based Analysis of Hologram Imagery and Aberrations, J. Opt. Soc. Am., Vol. 60, 1970, p. 715A.
19. D. J. Innes and A. L. Bloom, Spectra-Physics Laser Technical Bulletin No. 5, Spectra-Physics Corp., 1966.

UNCLASSIFIED
Security Classification

DOCUMENT CONTROL DATA - R & D

(Security classification of title, body of abstract and indexing annotation must be entered when the overall report is classified)

1. ORIGINATING ACTIVITY *(Corporate author)*
Willow Run Laboratories of the Institute of Science and Technology, The University of Michigan, Ann Arbor

2a. REPORT SECURITY CLASSIFICATION
Unclassified

2b. GROUP

3. REPORT TITLE
INVESTIGATION OF HOLOGRAPHIC TESTING TECHNIQUES

4. DESCRIPTIVE NOTES *(Type of report and inclusive dates)*
Semiannual Report, 1 June Through 27 November 1970

5. AUTHOR(S) *(First name, middle initial, last name)*
Emmett N. Leith and Charles M. Vest

6. REPORT DATE	7a. TOTAL NO. OF PAGES	7b. NO. OF REFS
February 1971	viii + 66	19

8a. CONTRACT OR GRANT NO.	9a. ORIGINATOR'S REPORT NUMBER(S)
DAAG46-69-C-0017 b. PROJECT NO. ARPA Order No. 1245 c. Program Code No. 8D10 d.	2420-21-P 9b. OTHER REPORT NO(S) *(Any other numbers that may be assigned this report)*

10. DISTRIBUTION STATEMENT

11. SUPPLEMENTARY NOTES

12. SPONSORING MILITARY ACTIVITY
Advanced Research Projects Agency
Department of Defense
Washington, D. C.

13. ABSTRACT

This report discusses holographic schemes for the detection of flaws in honeycomb panels and also describes the development of a method of reducing the sensitivity of holographic interferometry of transparent objects. An interferometric scheme for determining the surface roughness of flat objects is presented, and a planned application of the technique to curved objects is discussed. Recent advances in multiple-frequency holographic contouring are described, and a comparison of holographic and shadow-moiré contouring schemes is presented. A computer simulation of acoustical holography and its use for reduction of aberration are also discussed.

DD FORM 1 NOV 68 1473

UNCLASSIFIED
Security Classification

KEY WORDS	LINK A		LINK B		LINK C	
	ROLE	WT	ROLE	WT	ROLE	WT
Holographic testing Nondestruc'ive testing Interferometry Pulsed-laser holography Multiple-wavelength holography Acoustical holography						